Electronic Supplementary Material (ESI) for Dalton Transactions.
This journal is © The Royal Society of Chemistry 2022

Supporting Information

Multifunctional switching properties of "wire-like" dinuclear ruthenium bis-alkynyl spiropyran complexes.

David Jago,[a] Amelia R. Langley,[a,¶] Samantha G. Eaves,[a,‡] Mark C. Walkey,[a,] Thea Pulbrook,[a, ǀ] Stephen A. Moggach,[a] Paul J. Low,[*,a] Matthew J. Piggott,[a] George A. Koutsantonis[*,a]

[a] Chemistry, School of Molecular Sciences, University of Western Australia, Crawley, Western Australia 6009, Australia

[¶] Current address: Electrochemical Storage Team, imec/EnergyVille, Kapeldreef 75, 3001 Leuven, Belgium. Email: Amelia.r.Langley@outlook.com

[‡] Current address: TSG Consulting Ltd, Knaresborough, UK; email: s.g.symes1990@gmail.com

[ǀ] Current address: Hydro Tasmania, Hobart, TAS 7000; Email: Thea.pulbrook@gmail.com

Table of Contents

Phosphorus NMR....2
Electrochemistry....3
Spectroelectrochemistry....11
Crystallography....13
UV-vis spectroscopy and Acid Switching....15
Spectra....22
DFT Calculations....35

Phosphorus NMR

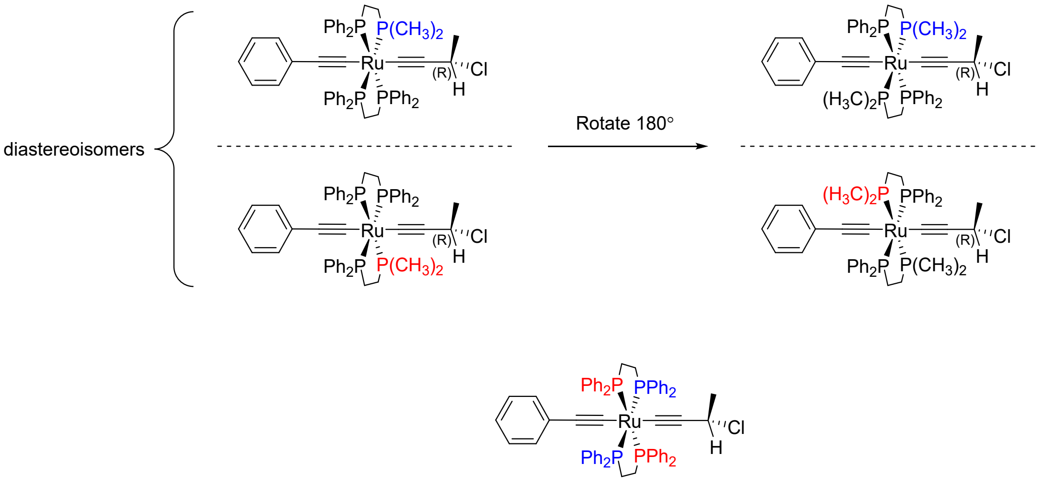

Figure S1 The introduction of a stereocentre makes the phosphino diastereotopic. If a diphenylphopshino groups cis to one anoth-er is replaced with another group ($P(CH_3)_2$ in this example), the relationship between the two isomers formed is diastereomeric.

Electrochemistry

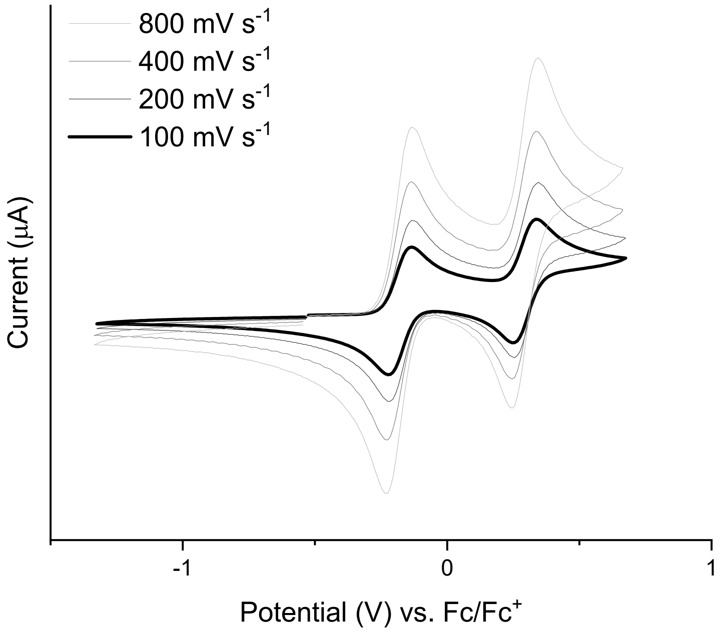

Figure S2 Cyclic Voltammogram of SP-**10** at various scan rates. All data were recorded in 0.1 M Bu_4NPF_6 CH_2Cl_2 using a Pt working electrode.

Table S1 Electrochemical Data for SP-**10.**

Scan Rate (mV s^{-1})	$\Delta E^{+/0}$ (V)	i_{pa}/i_{pc}	$\Delta E^{2+/+}$ (V)	i_{pa}/i_{pc}
100	0.08	0.95	0.09	1.07
200	0.10	0.94	0.09	1.07
400	0.09	0.94	0.09	1.06
800	0.10	0.94	0.09	1.06

All data were recorded in 0.1 M Bu_4NPF_6 CH_2Cl_2 using a Pt working electrode.

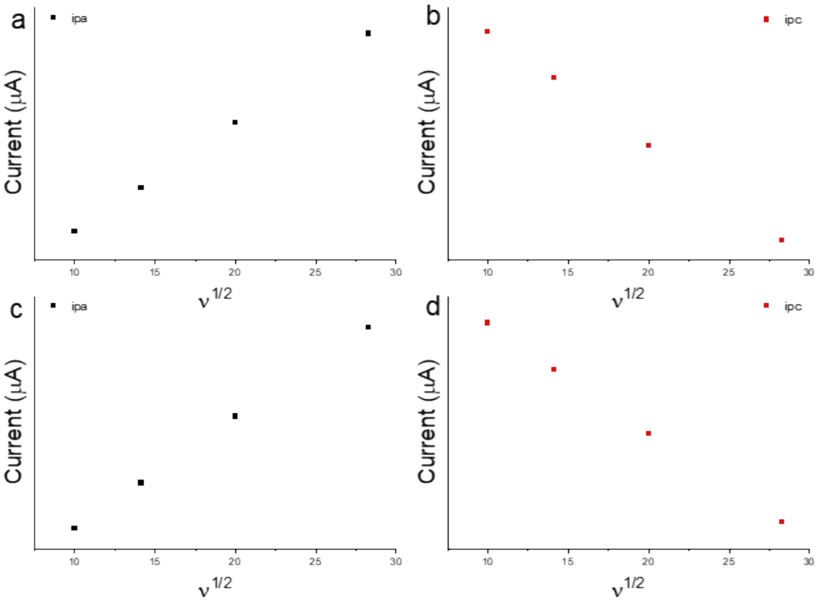

Figure S3 Plots of scan rate$(\nu)^{1/2}$ versus peak current (I_{pa} and I_{pc}) for the first oxidation (a,b) and the second oxidation (c,d) of SP-**10**. All data were recorded in 0.1 M Bu_4NPF_6 CH_2Cl_2 using a Pt working electrode.

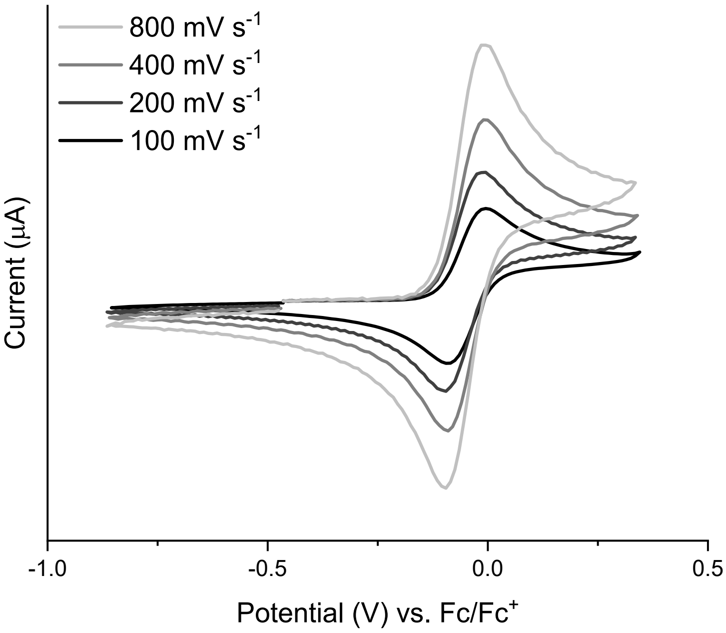

Figure S4 Cyclic Voltammogram of SP-**11** at various scan rates. All data were recorded in 0.1 M Bu_4NPF_6 CH_2Cl_2 using a Pt working electrode.

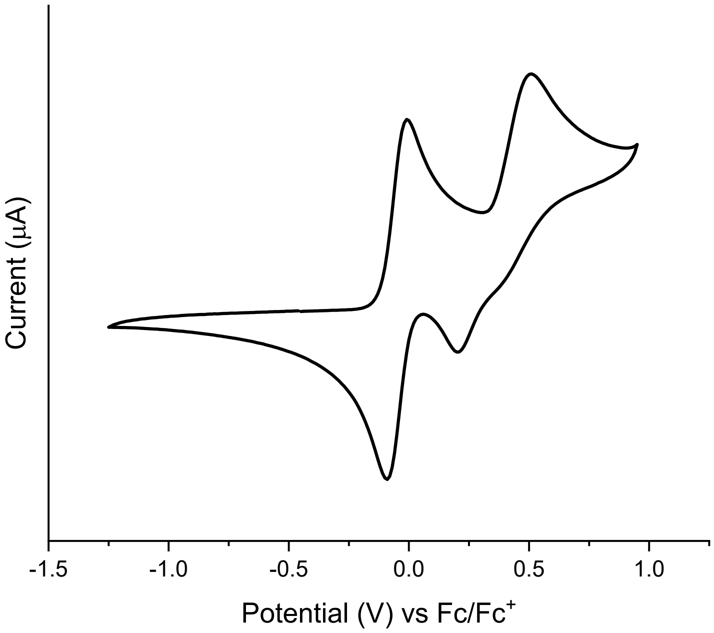

Figure S5 Cyclic Voltammogram of SP-**11** at 100 mV s^{-1}. All data were recorded in 0.1 M Bu_4NPF_6 in CH_2Cl_2 using a Pt working electrode.

Table S2 Electrochemical Data for SP-**11**.

Scan Rate (mV s-1)	$\Delta E^{+/0}(V)$	i_{pa}/i_{pc}	$\Delta E^{2+/+}(V)$	i_{pa}
100	0.09	0.96	0.31	0.35
200	0.09	0.94	0.33	0.50
400	0.08	0.95	0.35	0.72
800	0.09	0.96	0.40	1.03

All data were recorded in 0.1 M Bu_4NPF_6 CH_2Cl_2 using a Pt working electrode.

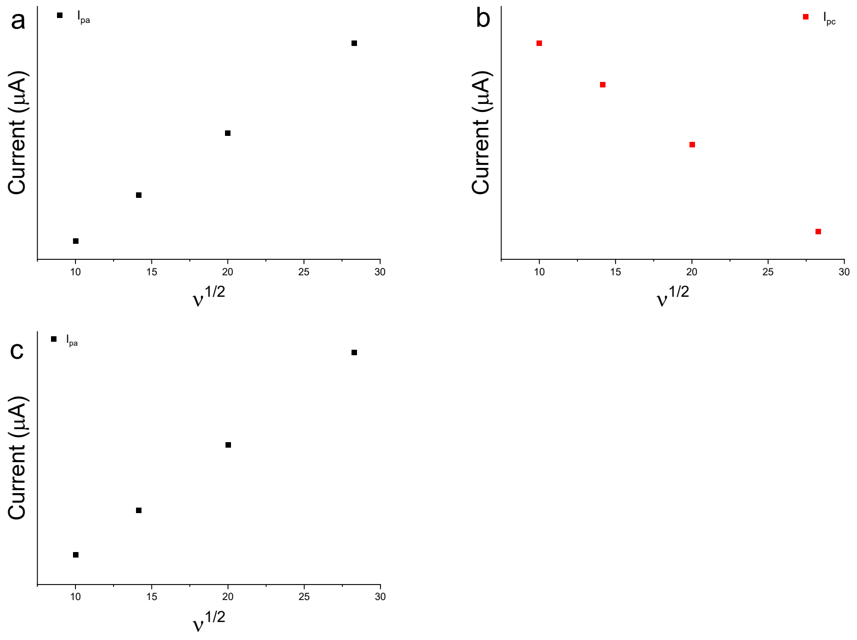

Figure S6 Plots of scan rate(v)$^{1/2}$ versus peak current (I_{pa} (a) and I_{pc} (b)) for the first oxidation of SP-**11** and peak current (I_{pa}) for the second oxidation (c) of complex SP-**11**. All data were recorded in 0.1 M Bu_4NPF_6 CH_2Cl_2 using a Pt working electrode.

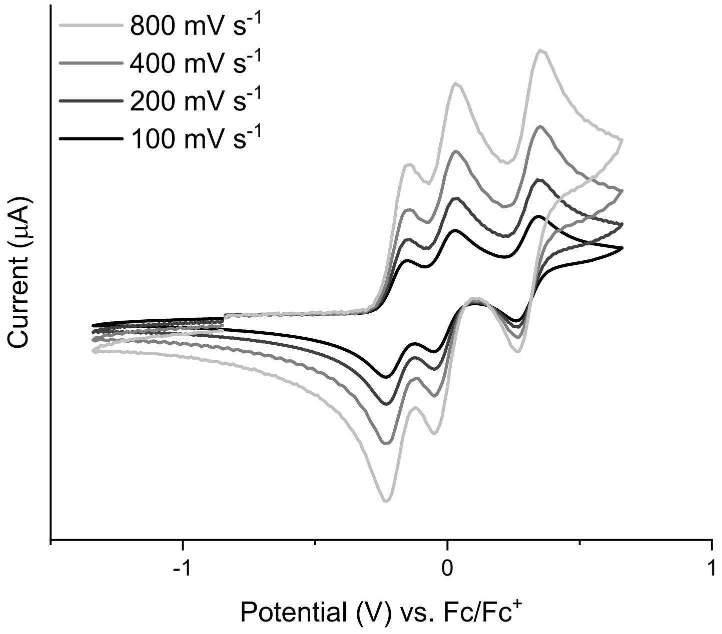

Figure S7 Cyclic Voltammogram of SP-**13** at various scan rates. All data were recorded in 0.1 M Bu_4NPF_6 CH_2Cl_2 using a Pt working electrode.

Table S3 Electrochemical Data for SP-**13**.

Scan Rate (mV s-1)	$\Delta E^{+/0}$(V)	i_{pa}	$\Delta E^{2+/+}$(V)	i_{pc}	$\Delta E^{3+/2+}$(V)	i_{pa}/i_{pc}
100	0.08	0.25	0.09	0.22	0.08	0.86
200	0.08	0.35	0.09	0.31	0.08	0.81
400	0.08	0.50	0.09	0.45	0.08	0.82
800	0.08	0.73	0.08	0.62	0.08	0.81

All data were recorded in 0.1 M Bu_4NPF_6 CH_2Cl_2 using a Pt working electrode.

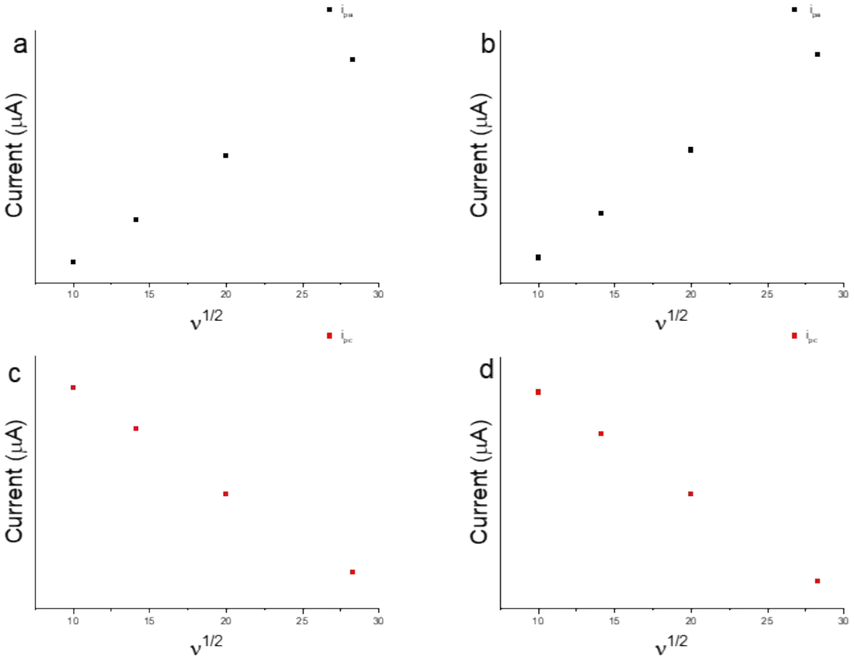

Figure S8 Plots of scan rate (v)$^{1/2}$ versus peak current (ipa) for the first oxidation (a) and the third oxidation (b) and the peak current (ipc) for the second oxidation (c) and the third oxidation (d) of SP-**13**. All data were recorded in 0.1 M Bu_4NPF_6 CH_2Cl_2 using a Pt working electrode.

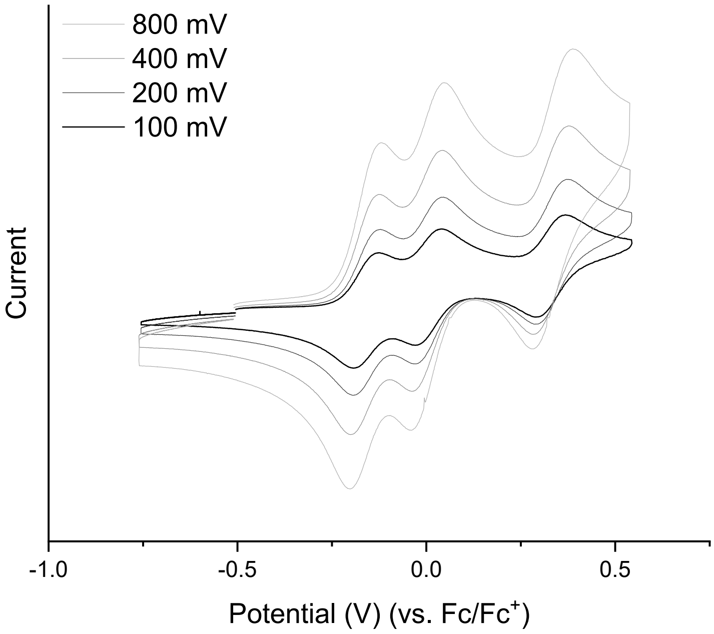

Figure S9 Cyclic Voltammogram of SP-**16** at various scan rates. All data were recorded in 0.1 M Bu_4NPF_6 CH_2Cl_2 using a Pt working electrode.

Table S4 Electrochemical Data for SP-**16**.

Scan Rate (mV s^{-1})	$\Delta E^{+/0}$(V)	i_{pa}	$\Delta E^{2+/+}$ (V)	i_{pc}	$\Delta E^{3+/2+}$ (V)	i_{pa}/i_{pc}
100	0.07	1.17	0.07	0.90	0.08	1.03
200	0.07	1.62	0.08	1.26	0.08	1.16
400	0.08	2.25	0.08	1.71	0.09	1.11
800	0.08	3.06	0.09	2.43	0.10	1.36

All data were recorded in 0.1 M Bu_4NPF_6 CH_2Cl_2 using a Pt working electrode.

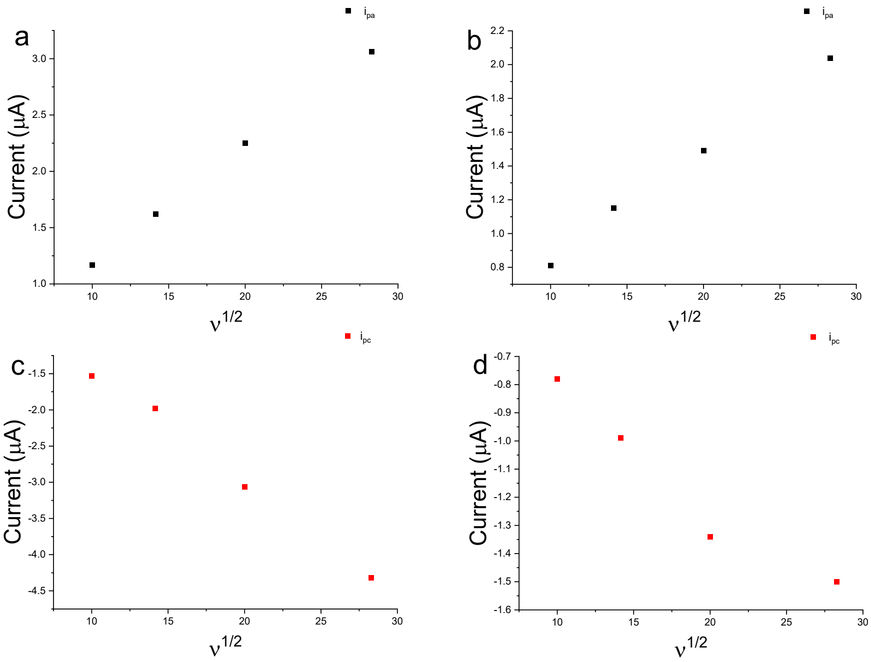

Figure S10 Plots of scan rate $(v)^{1/2}$ versus peak current (ipa) for the first oxidation (a) and the third oxidation (b) and the peak current (ipc) for the second oxidation (c) and the third oxidation (d) of SP-**16**. All data were recorded in 0.1 M Bu_4NPF_6 CH_2Cl_2 using a Pt working electrode.

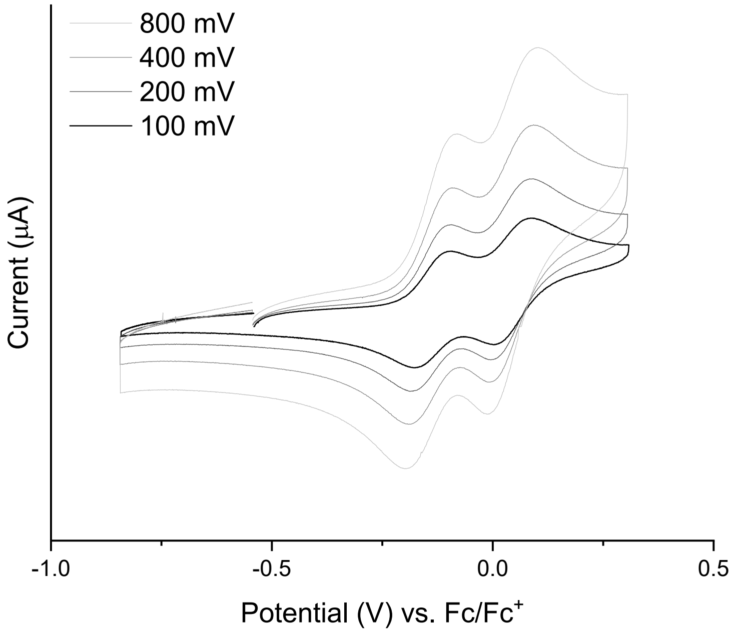

Figure S11 Cyclic Voltammogram of SP-**18** at various scan rates. All data were recorded in 0.1 M Bu_4NPF_6 CH_2Cl_2 using a Pt working electrode.

Table S5 Electrochemical Data for SP-**18**.

Scan Rate (mV s^{-1})	$\Delta E^{+/0}$(V)	i_{pa}	$\Delta E^{2+/+}$(V)	i_{pc}
100	0.08	0.63	0.08	0.66
200	0.09	0.94	0.09	0.90
400	0.10	1.28	0.10	1.17
800	0.12	1.80	0.12	1.58

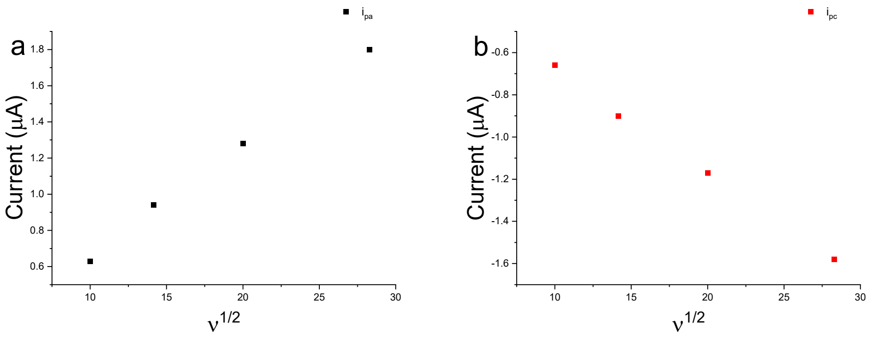

All data were recorded in 0.1 M Bu_4NPF_6 CH_2Cl_2 using a Pt working electrode.

Figure S12 Plots of scan rate (v)$^{1/2}$ versus peak current (ipa) for the first oxidation (a) and the peak current (ipc) for the second oxidation (b) of SP-**18**. All data were recorded in 0.1 M Bu_4NPF_6 CH_2Cl_2 using a Pt working electrode.

Spectroelectrochemistry

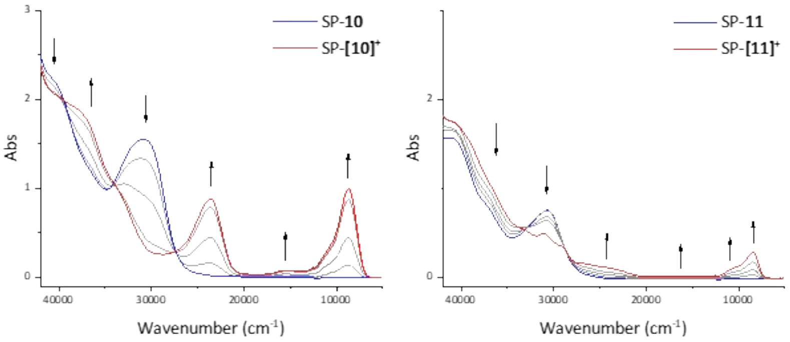

Figure S13 UV-vis-NIR spectra changes upon oxidation of complexes SP-**10** and SP-**11** to SP-[**10**]$^+$ and SP-[**11**]$^+$. All data were recorded in 0.1 M Bu_4NPF_6 CH_2Cl_2 using a Pt working electrode.

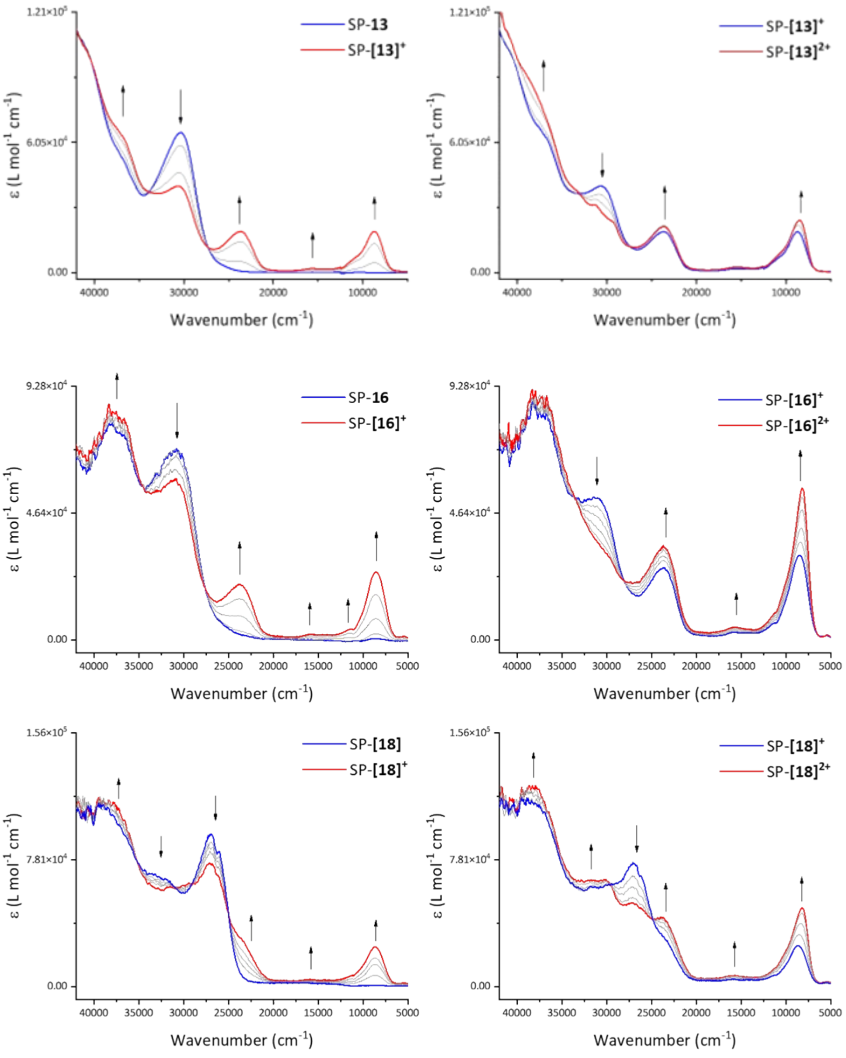

Figure S14 UV-vis-NIR spectra changes upon oxidation of complexes **13**, **16** and **18** to [**13**]$^+$, [**16**]$^+$ and [**18**]$^+$, and [**13**]$^{2+}$, [**16**]$^{2+}$ and [**18**]$^{2+}$. All data were recorded in 0.1 M Bu_4NPF_6 CH_2Cl_2 using a Pt working electrode.

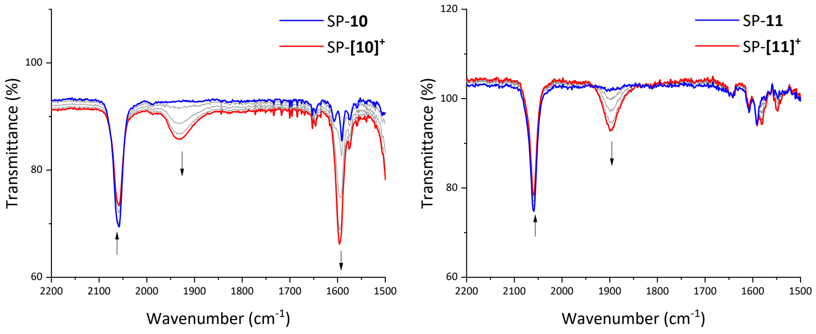

Figure S15 IR spectra changes upon oxidation of complexes SP-**10** and SP-**11** to SP-[**10**]+ and SP-[**11**]$^+$. All data were recorded in 0.1 M Bu_4NPF_6 CH_2Cl_2 using a Pt working electrode.

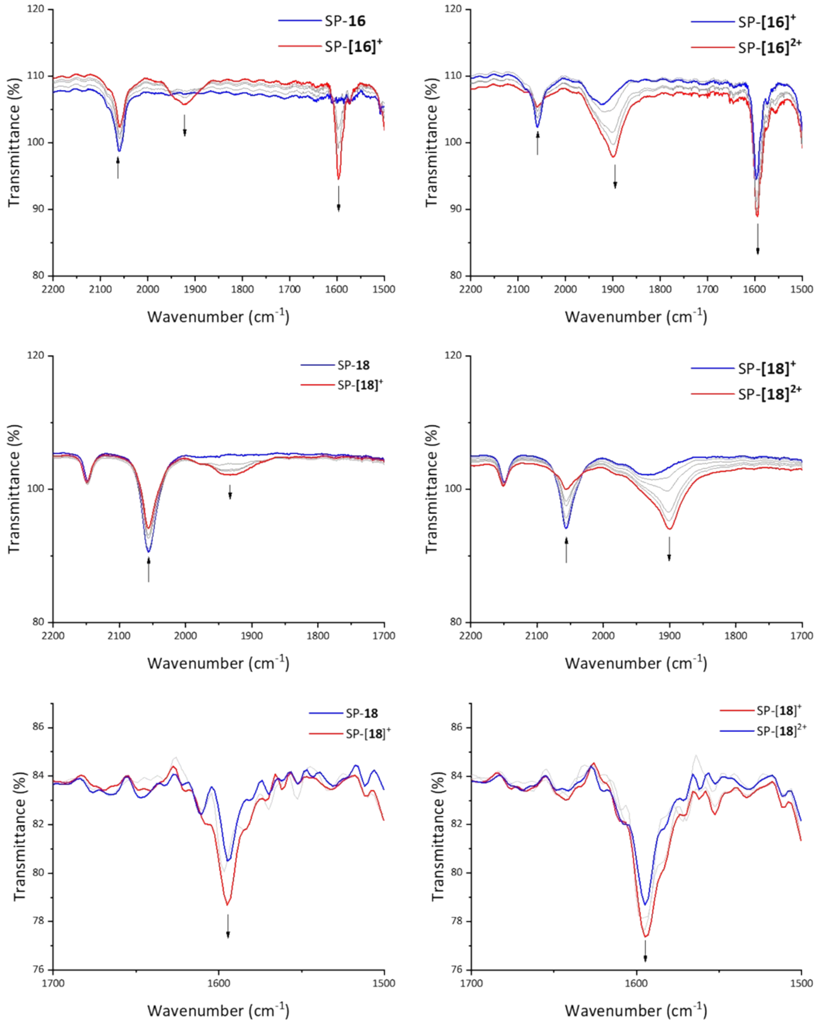

Figure S16 IR spectra changes upon oxidation of complexes SP-**16** and SP-**18** to SP- [**16**]$^+$ and SP-[**18**]$^+$, and SP-[**16**]$^{2+}$ and SP-[**18**]$^{2+}$. All data were recorded in 0.1 M Bu_4NPF_6 CH_2Cl_2 using a Pt working electrode.

Crystallography

Table S6. Crystal Data and structure refinement

Compound	**SP-10**	**SP-13**

Crystal data

Chemical formula	$C_{81}H_{71}NOP_4Ru{\cdot}2(C_4H_{10}O){\cdot}0.5(H_2O)$	$C_{143}H_{123}NOP_8Ru_2{\cdot}CH_2Cl_2{\cdot}3[CH2Cl_2]$
***M*$_r$**	1456.58	2661.02
Crystal system, space group	Monoclinic, $P2_1$	Triclinic, $P\bar{1}$
***a*, *b*, *c* (Å)**	9.4183 (1), 31.4732 (2), 13.0007 (1)	9.8197 (3), 12.7046 (4), 54.4568 (17)
a, b, γ (°)	90, 104.668 (1), 90	85.315 (3), 88.454 (3), 73.248 (3)
***V* (Å^3)**	3728.12 (6)	6483.7 (4)
μ (mm^{-1})	2.91	4.74
Crystal size (mm)	0.25 × 0.13 × 0.13	0.18 × 0.07 × 0.05

Data collection

Absorption correction	Gaussian *CrysAlis PRO* 1.171.41.103a (Rigaku Oxford Diffraction, 2021) Numerical absorption correction based on gaussian integration over a multifaceted crystal model Empirical absorption correction using spherical harmonics, implemented in SCALE3 ABSPACK scaling algorithm.	Analytical *CrysAlis PRO* 1.171.41.103a (Rigaku Oxford Diffraction, 2021) Analytical numeric absorption correction using a multifaceted crystal model based on expressions derived by R.C. Clark & J.S. Reid. (Clark, R. C. & Reid, J. S. (1995). Acta Cryst. A51, 887-897) Empirical absorption correction using spherical harmonics, implemented in SCALE3 ABSPACK scaling algorithm.
***T*$_{min}$, *T*$_{max}$**	0.613, 1.000	0.816, 0.922
No. of measured, independent and observed [*I* > 2s(*I*)] reflections	71086, 14932, 14198	41885, 41885, 33140
***R*$_{int}$**	0.053	0.1517
(sin q/l)$_{max}$ (Å^{-1})	0.628	0.595

Refinement

$R[F^2 > 2s(F^2)]$, $wR(F^2)$, S	0.045, 0.121, 1.04	0.174, 0.390, 1.07
No. of reflections	14932	41885
No. of parameters	863	521
No. of restraints	19	1210
	$w = 1/[s^2(F_o^2) + (0.0703P)^2 + 4.3486P]$ where $P = (F_o^2 + 2F_c^2)/3$	$w = 1/[s^2(F_o^2) + (0.0829P)^2 + 171.2715P]$ where $P = (F_o^2 + 2F_c^2)/3$
$\Delta\rho_{max}$, $\Delta\rho_{min}$ (e Å^{-3})	1.90, -0.67	3.13, -2.31
Absolute structure	Refined as an inversion twin.	–
Absolute structure parameter	0.430 (9)	–

Computer programs: *CrysAlis PRO* 1.171.41.103a (Rigaku OD, 2021), *SHELXT* 2018/2 (Sheldrick, 2018), XS (Sheldrick, 2008), XL (Sheldrick, 2008), Olex2 1.5 (Dolomanov *et al.*, 2009).

UV-vis spectroscopy and Acid Switching

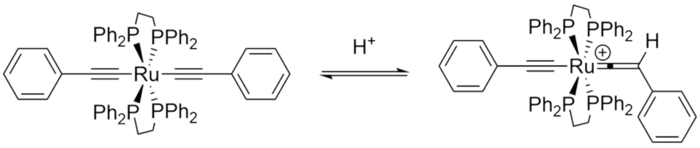

19 **19-H$^+$**

Figure S17 Protonation of **19**.

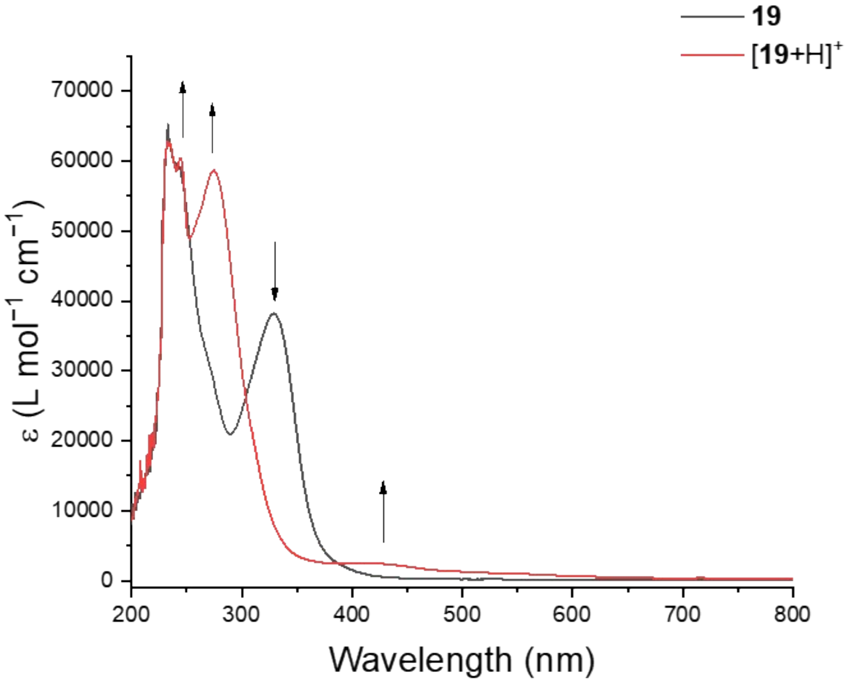

Figure S18 UV-vis spectral changes accompanying the addition of TFA to a CH_2Cl_2 solution of **19**.

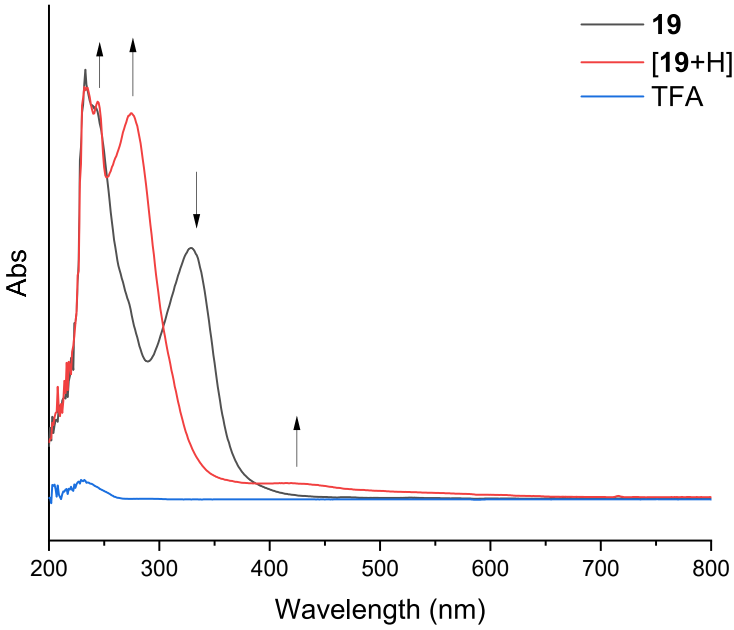

Figure S19 UV-vis spectral changes accompanying the addition of TFA to a CH_2Cl_2 solution of **19** with absorbance of TFA overlayed.

Table S7 Absorbance peaks (λ_{max}) for **19** (in CH_2Cl_2) and its protonated vinylidene form.

Complex	Absorbance /λ_{max} (nm) (ε /L mol^{-1} cm^{-1})
19	239 (59,000), 329 (38,000)
[**19**+H]$^+$	234 (62,000), 244 (60,000), 275 (59,000), 416 (2500)

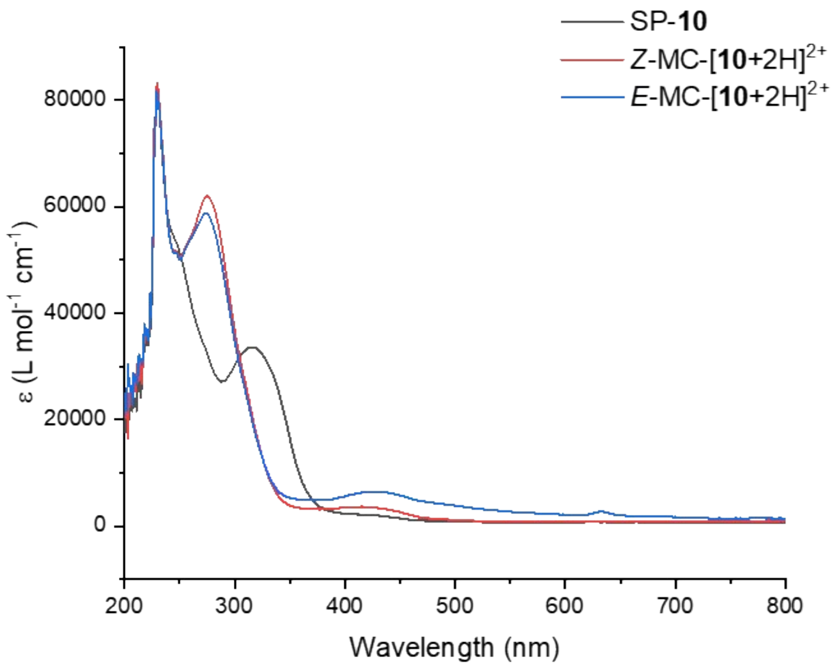

Figure S20 UV-vis spectral changes accompanying the addition of excess TFA to a CH_2Cl_2 solution of SP-**10** and subsequent exposure to UV light.

Table S8 Absorbance peaks (λ_{max}) for SP-**10** (in CH_2Cl_2) and its protonated states.

Complex	Absorbance /λ_{max} (nm) (ε /L mol^{-1} cm^{-1})
SP-**10**	230 (82,000), 315(33,000)
Z-MC-[**10**+2H]$^{2+}$	230 (83,000), 275 (62,000), 414 (3800)
E-MC-[**10**+2H]$^{2+}$	230 (82,000), 275 (58,000), 427 (64,000), 633 (2800)
SP-[**10**+H]$^{+}$	275, 417
E-MC-[**10**+H]$^{+}$	275, 421, 622

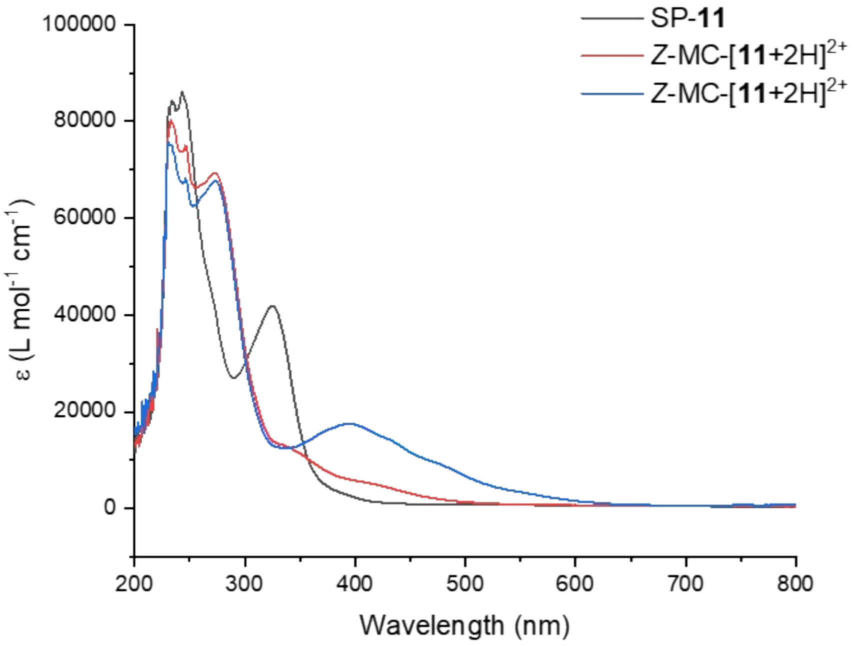

Figure S21 UV-vis spectral changes accompanying the addition of excess TFA to a CH_2Cl_2 solution of SP-**11** and subsequent exposure to UV light.

Table S9 Absorbance peaks (λ_{max}) for SP-**11** (in CH_2Cl_2) and its protonated states.

Complex	Absorbance /λ_{max} (nm) (ε /L mol^{-1} cm^{-1})
SP-**11**	244 (86,000), 325(42,000)
Z-MC-[**11**+2H]$^{2+}$	247 (75,000), 273 (69,000), 337 (13,000), 400 (5300)
E-MC-[**11**+2H]$^{2+}$	247 (68,000), 274 (68,000), 395 (17,000)

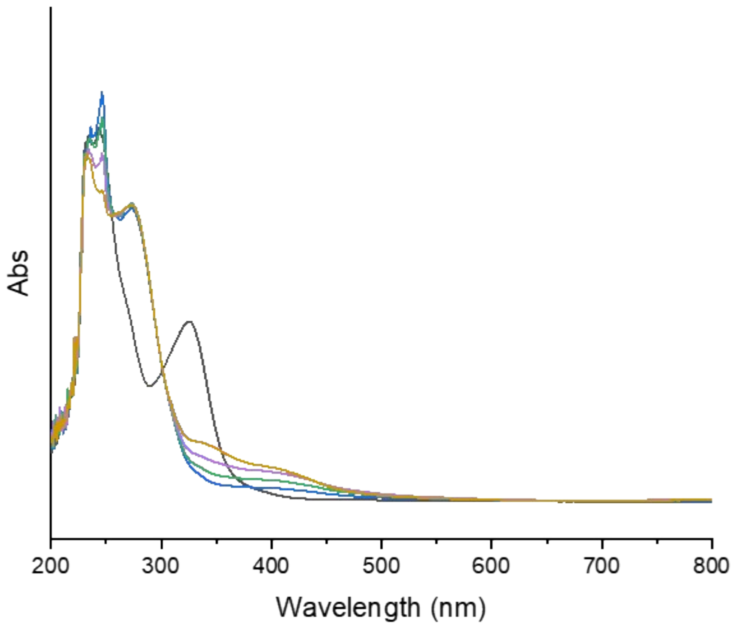

Figure S22 UV-vis spectral changes accompanying the addition of an equivalent and subsequent excess of TFA to a CH_2Cl_2 solution of SP-**11**

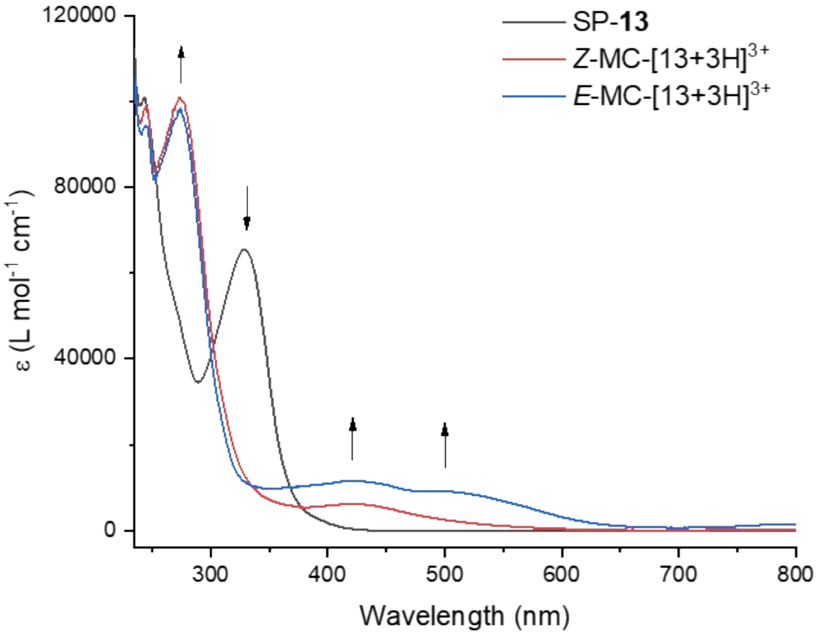

Figure S23 UV-vis spectral changes accompanying the addition of excess TFA to a CH_2Cl_2 solution of SP-**13** and subsequent exposure to UV light.

Table S9 Absorbance peaks (λ_{max}) for SP-**13** (in CH_2Cl_2) and its protonated states.

Complex	Absorbance /λ_{max} (nm) (ε /L mol^{-1} cm^{-1})
SP-**13**	244 (100,000), 329 (65,000)
Z-MC-[**13+3H**]$^{3+}$	244 (98,000), 275 (100,000), 422 (5800)
E-MC-[**13+3H**]$^{3+}$	244 (94,000), 275 (97,000), 422 (12,000), 500 (9300)

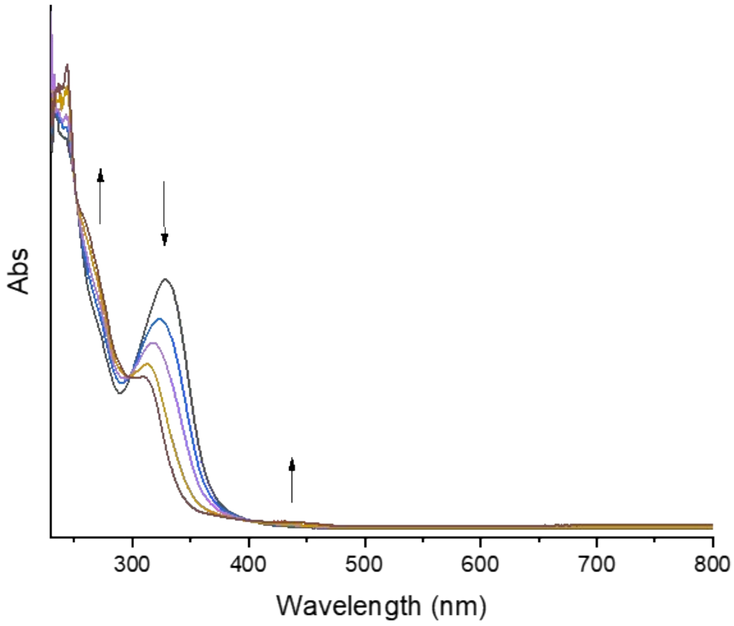

Figure S24 UV-vis changes accompanying the attempted titration of a CH_2Cl_2 solution of SP-**13** with TFA.

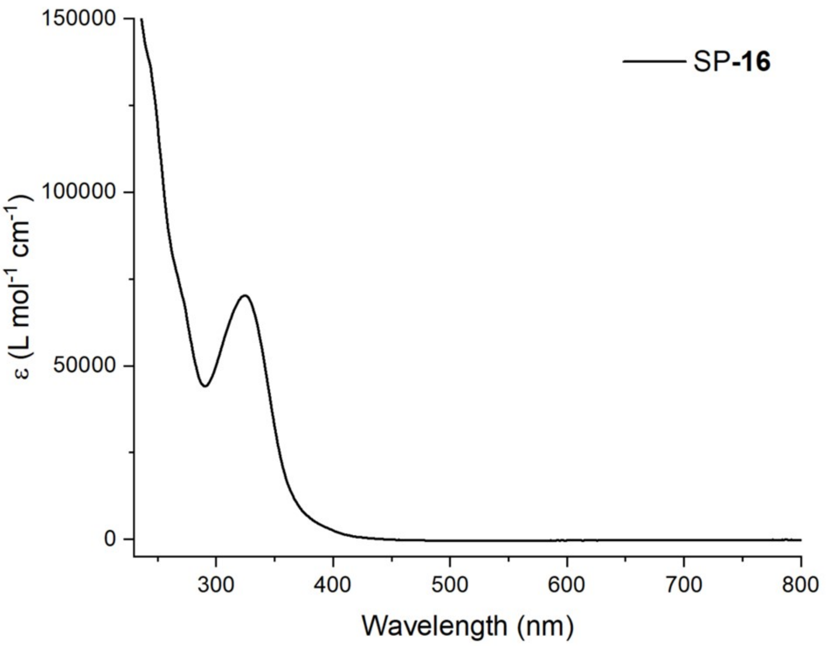

Figure S25 UV-vis spectrum of a CH_2Cl_2 solution of SP-**16**.

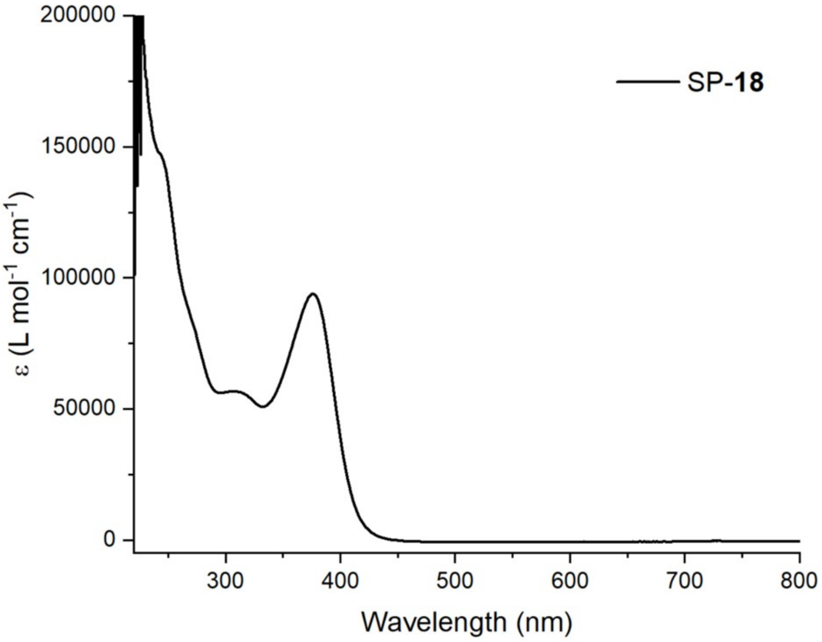

Figure S26 UV-vis spectrum of a CH_2Cl_2 solution of SP-**18**.

Table S10 Absorbance peaks (λ_{max}) for SP-**13** (in CH_2Cl_2) and its protonated states.

Complex	Absorbance /λ_{max} (nm) (ε /L mol^{-1} cm^{-1})
SP-**16**	243 (140,000), 323 (70,000)
SP-**18**	242 (147,000), 309 (57,000), 376 (94,000)

Spectra

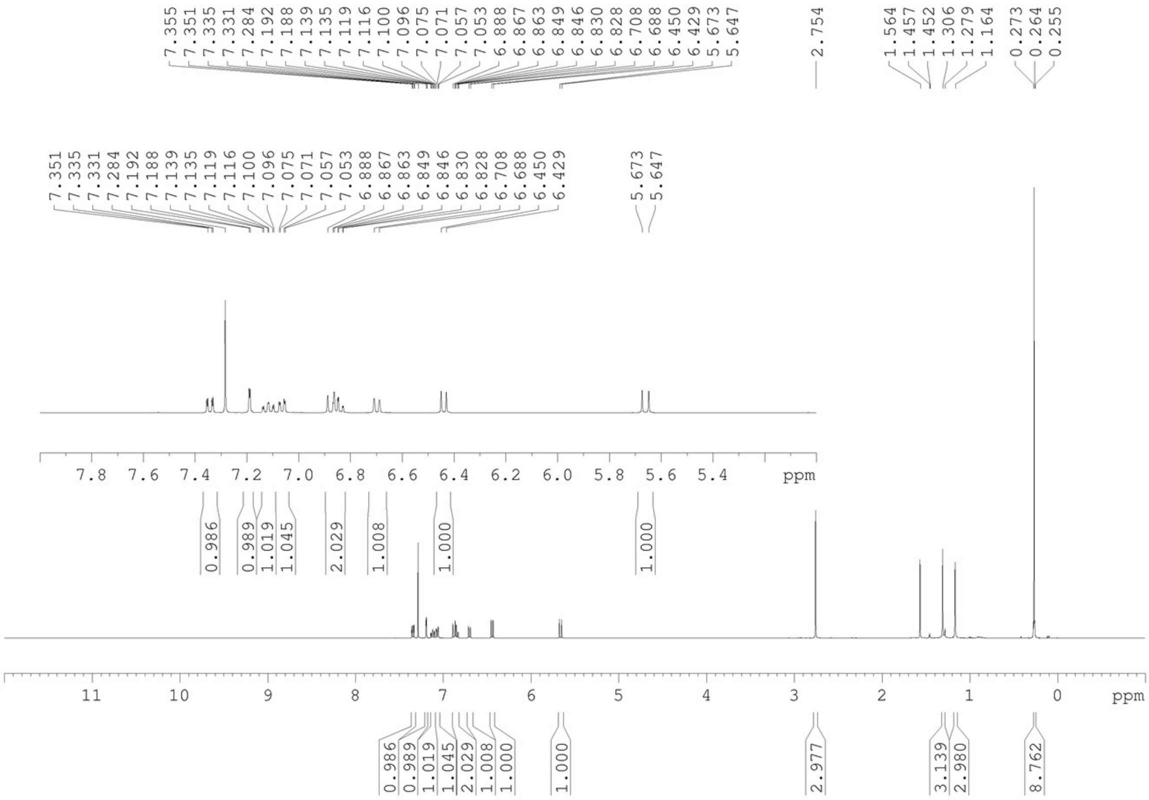

Figure S27 ^{1}H NMR (400 MHz) of **2** in $CDCl_3$

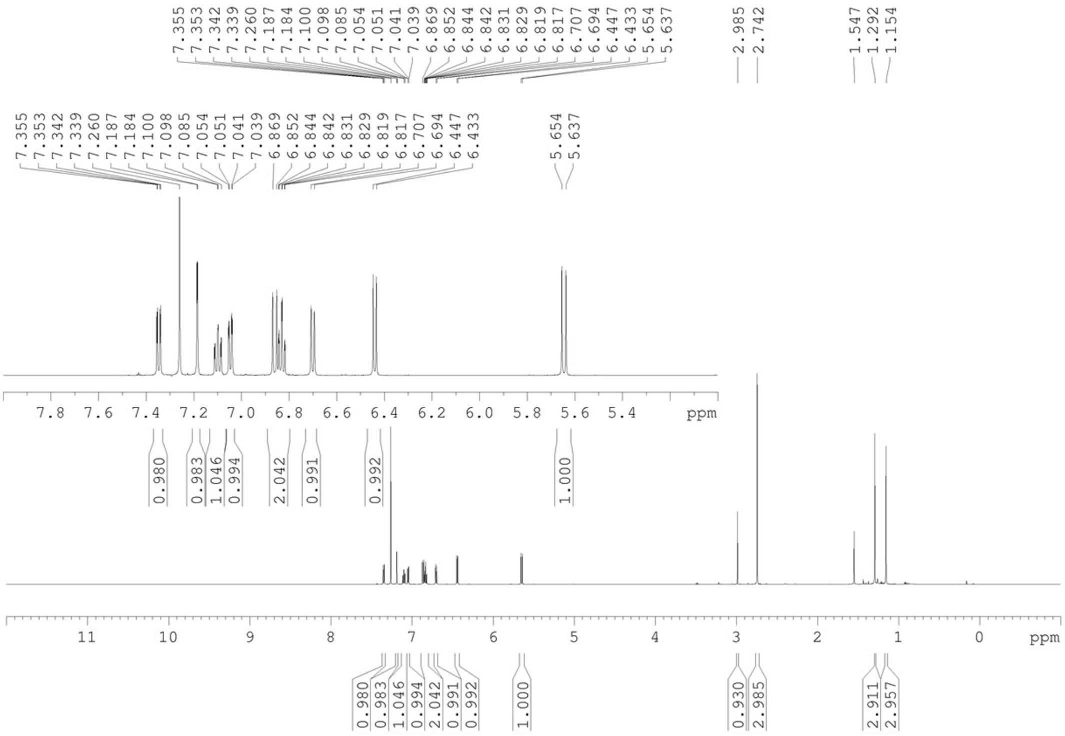

Figure S28 ^{1}H NMR (600 MHz) of **3** in $CDCl_3$

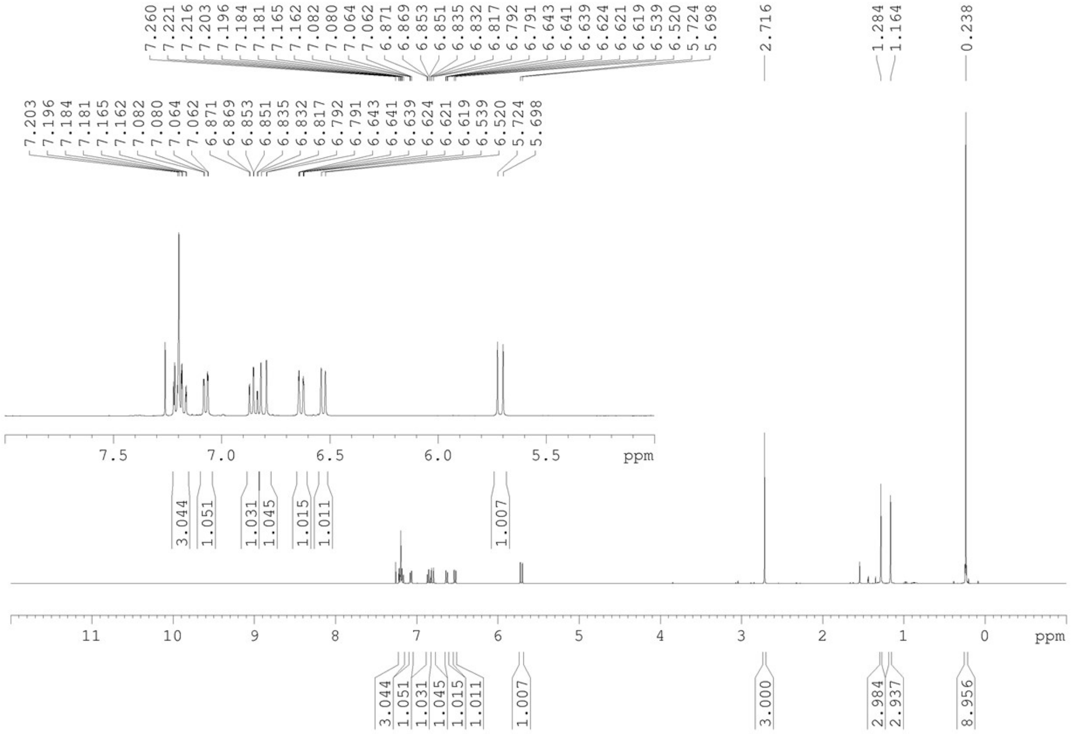

Figure S29 ^{1}H NMR (400 MHz) of **6** in $CDCl_3$

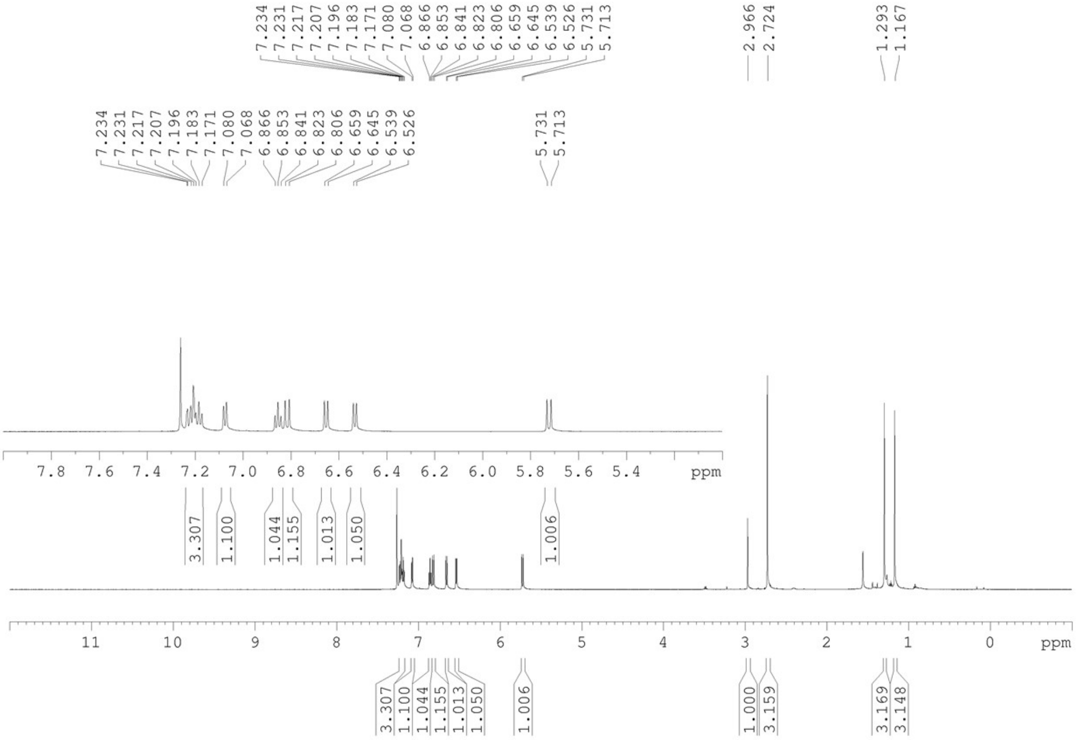

Figure S30 ^{1}H NMR (600 MHz) of **7** in CDCl$_3$

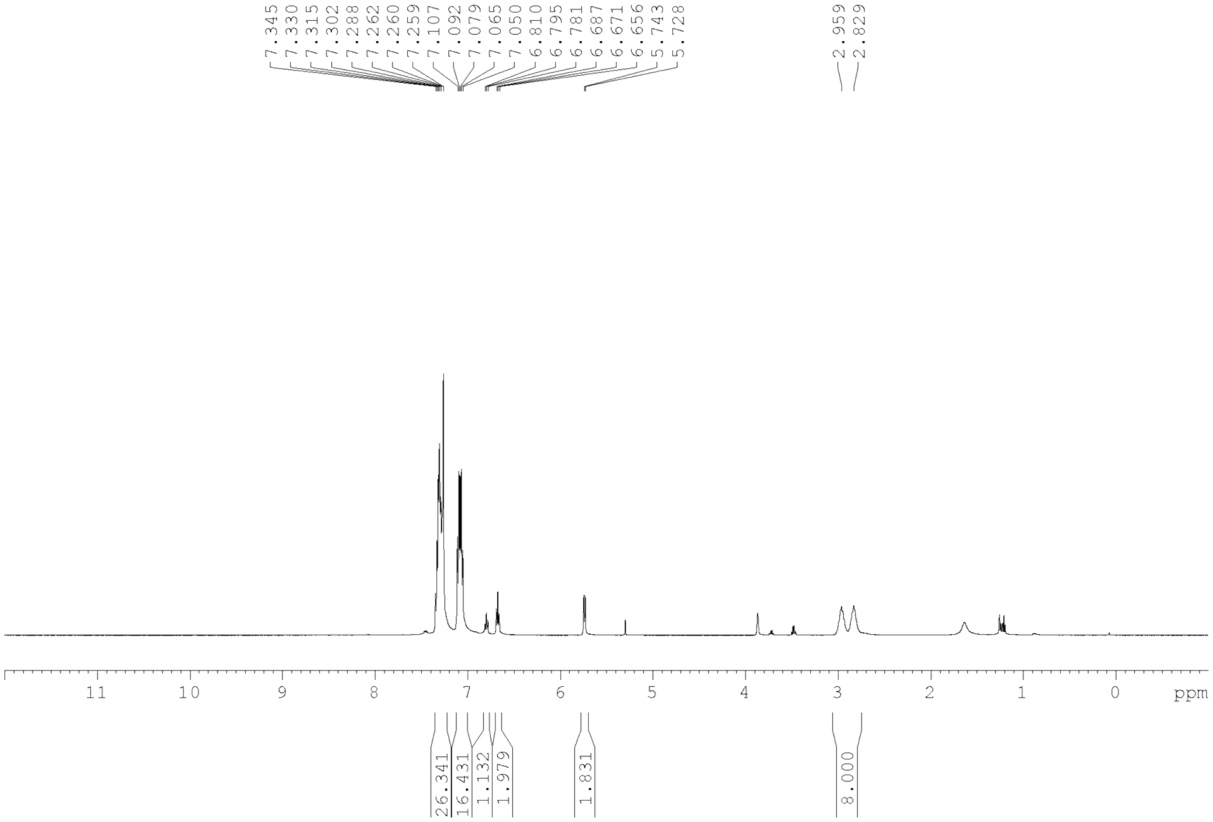

Figure S31 ^{1}H NMR (500 MHz) of **9** in CDCl$_3$

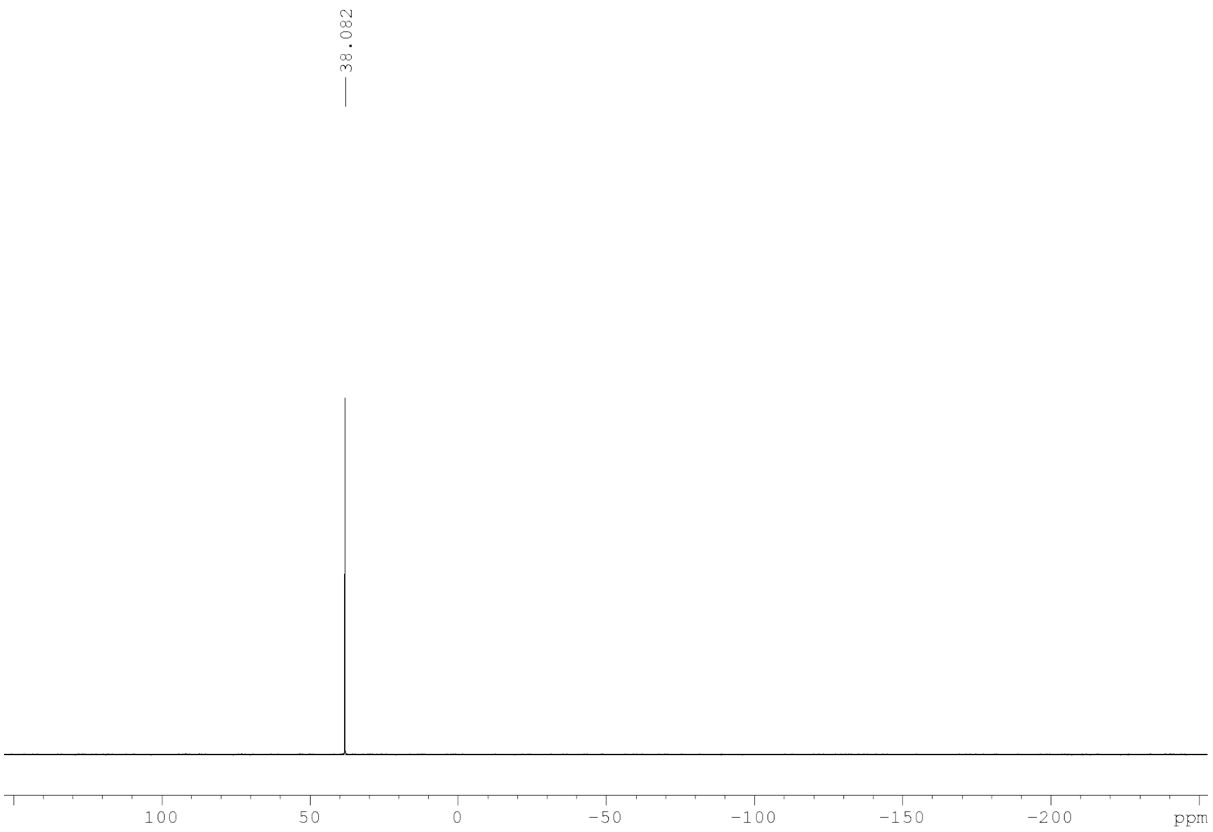

Figure S32 $^{31}P\{^1H\}$ NMR (400 MHz) of **9** in $CDCl_3$

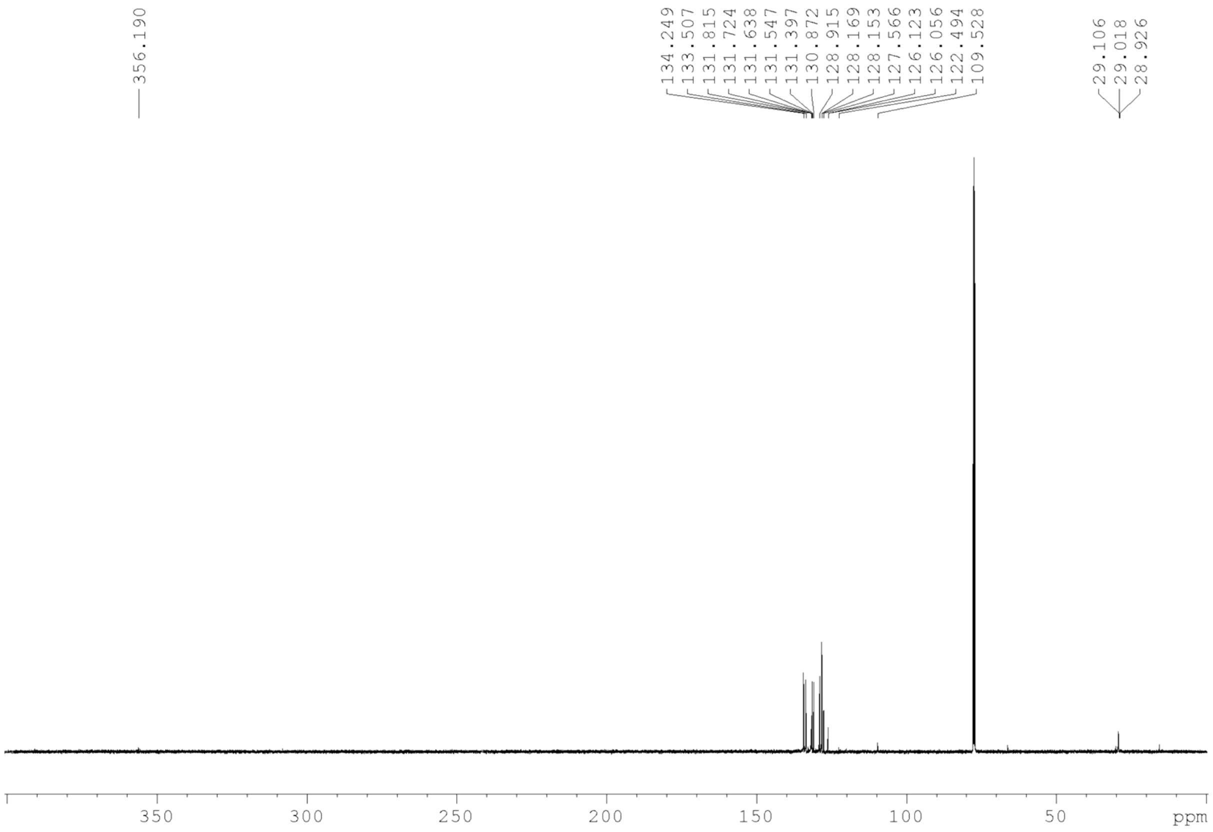

Figure S33 $^{13}C\{^1H\}$ NMR (500 MHz) of **9** in $CDCl_3$

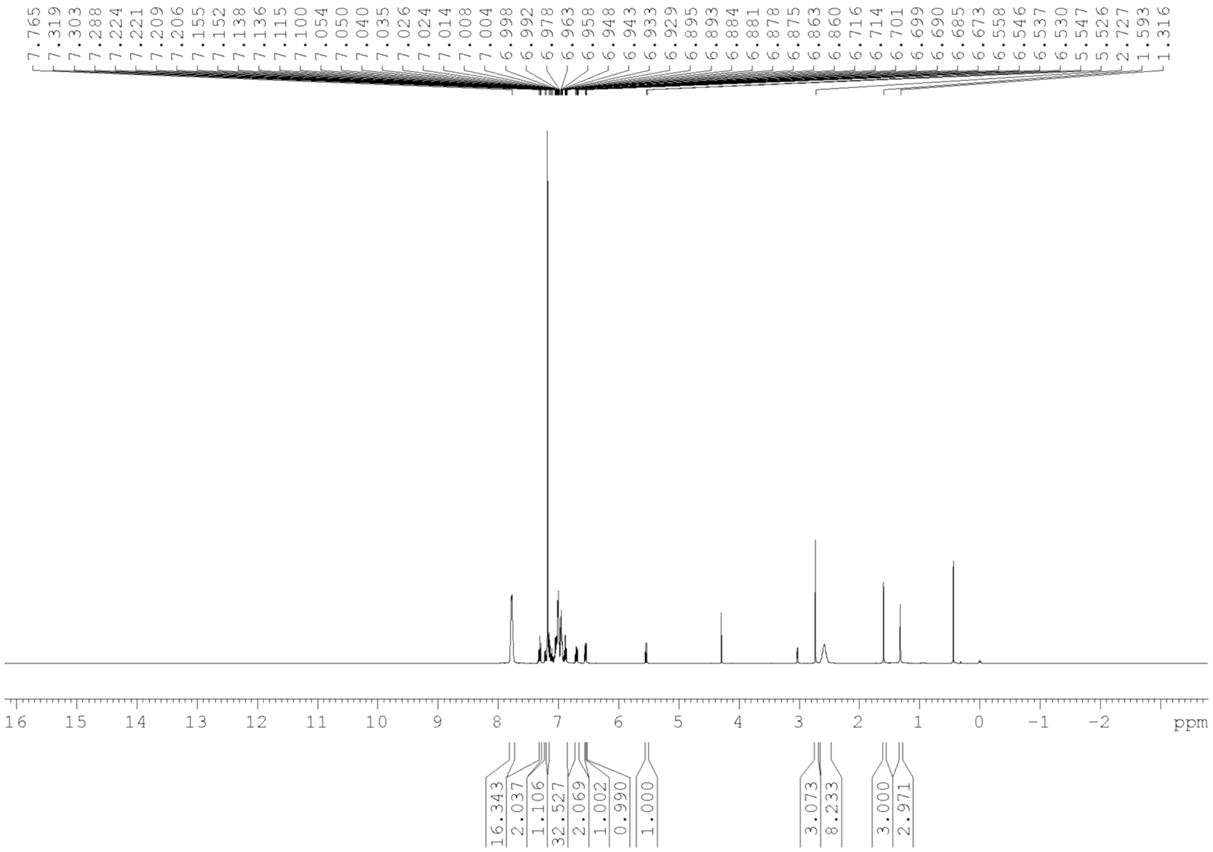

Figure S34 ^{1}H NMR (500 MHz) of SP-**10** in C_6D_6

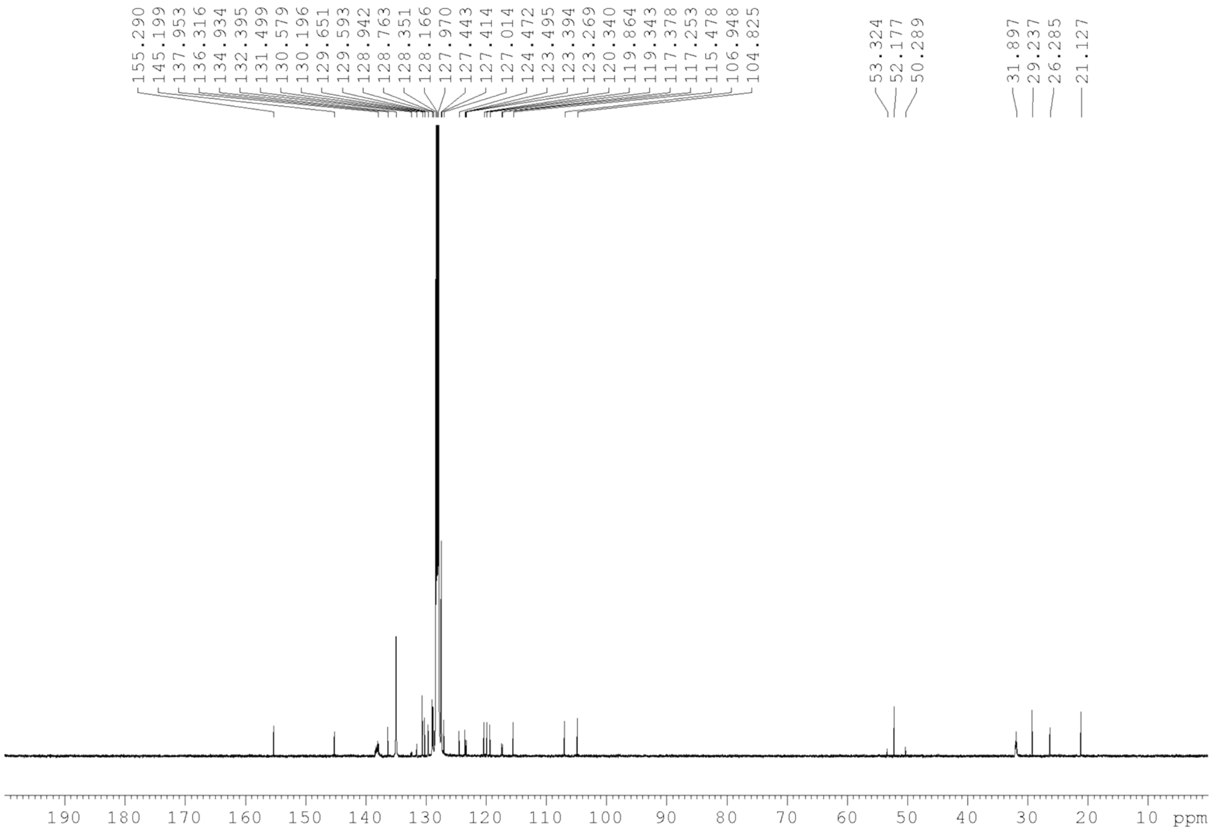

Figure S35 $^{13}C\{^1H\}$ NMR (500 MHz) of SP-**10** in C_6D_6

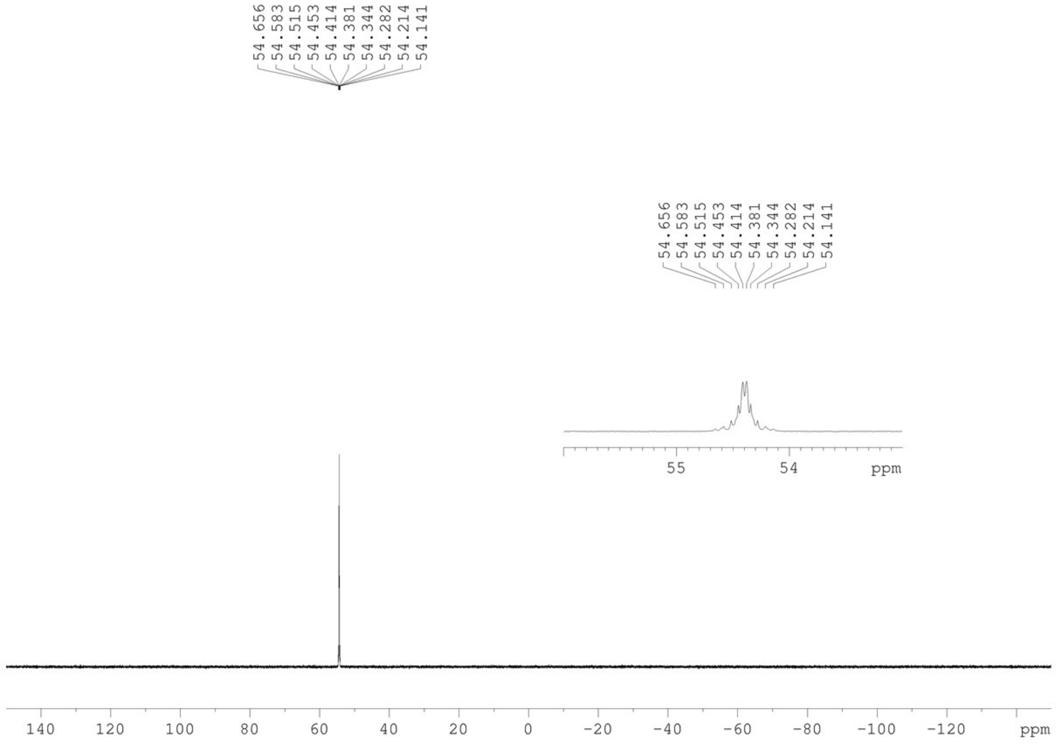

Figure S36 $^{31}P\{^1H\}$ NMR (500 MHz) of SP-**10** in C_6D_6

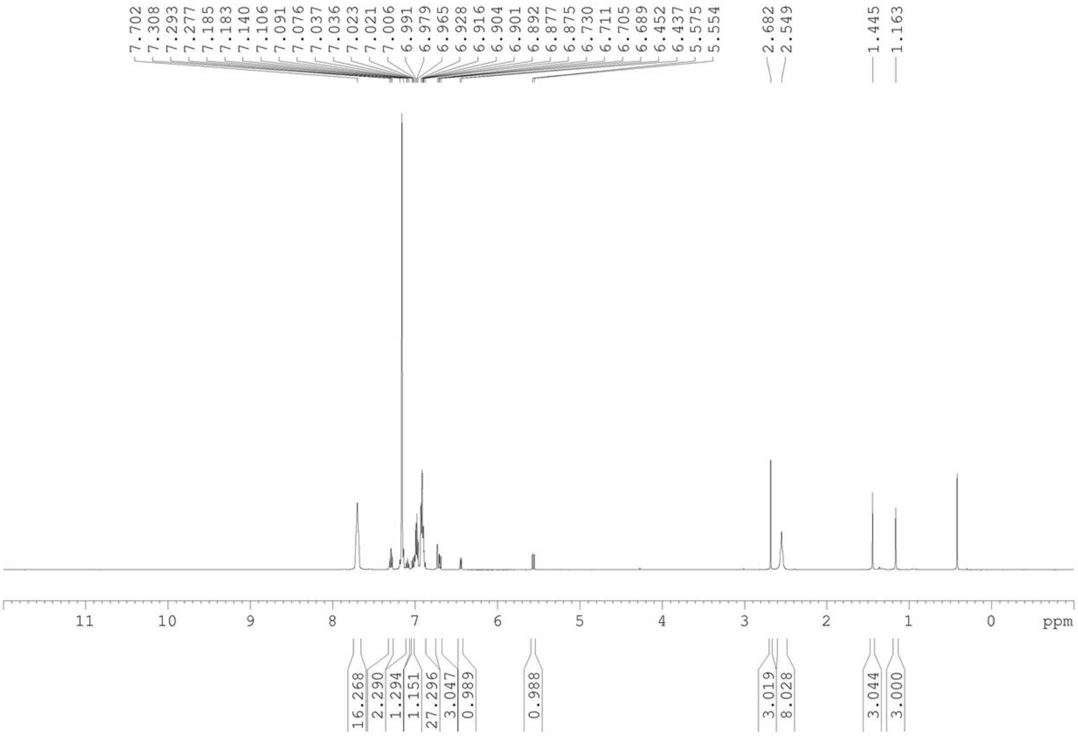

Figure S37 ^1H NMR (500 MHz) of SP-**11** in C_6D_6

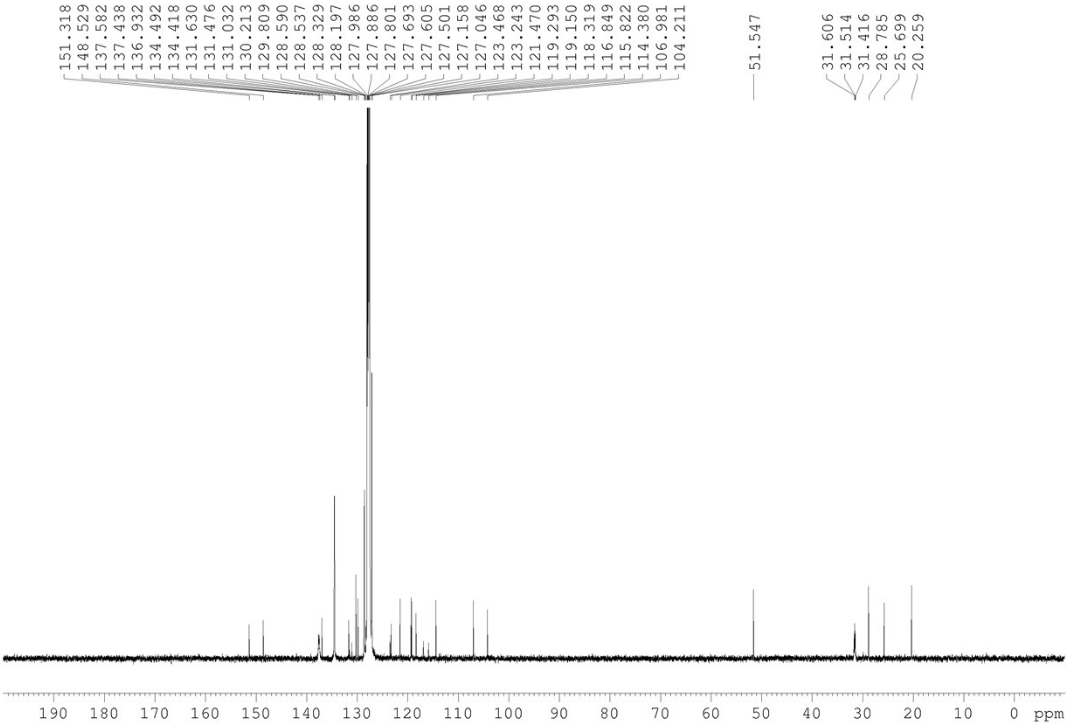

Figure S38 $^{13}C\{^1H\}$ NMR (500 MHz) of SP-**11** in C_6D_6

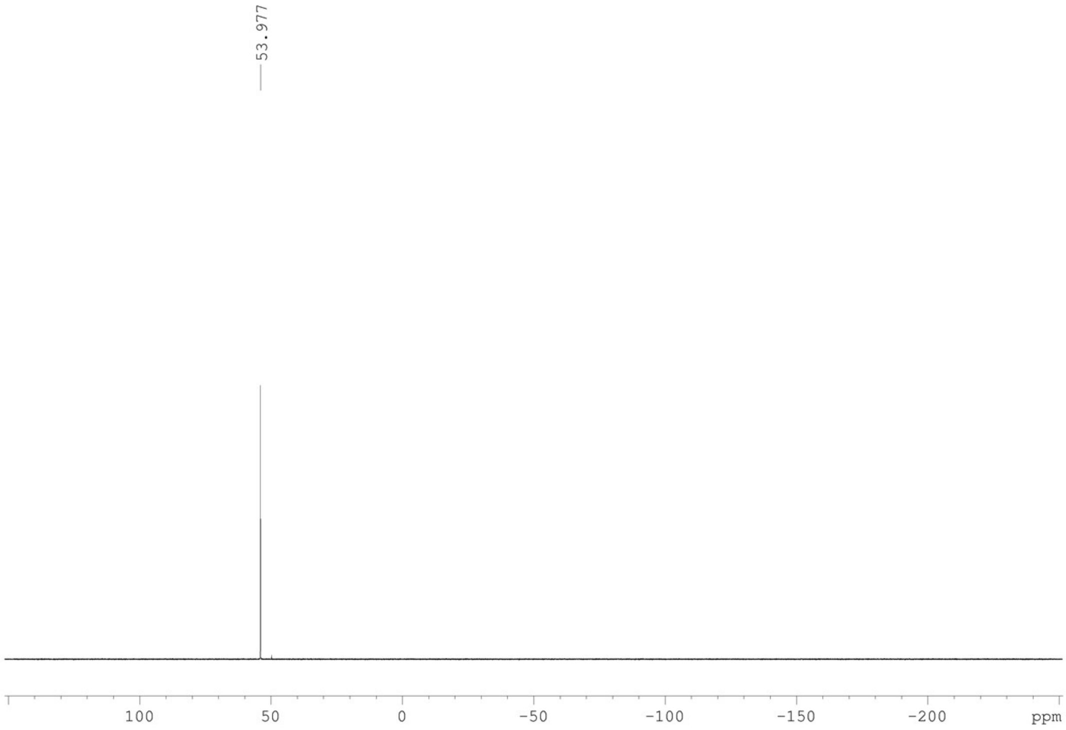

Figure S39 $^{31}P\{^1H\}$ NMR (500 MHz) of SP-**11** in C_6D_6

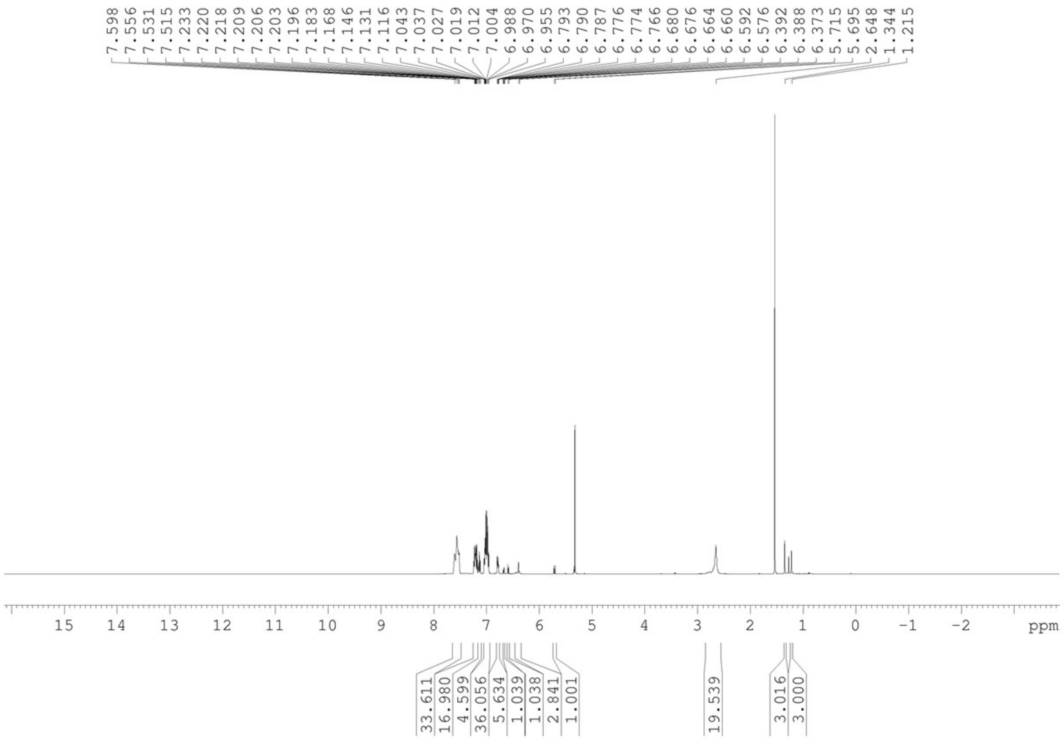

Figure S40 ^{1}H NMR (500 MHz) of SP-**13** in CD_2Cl_2

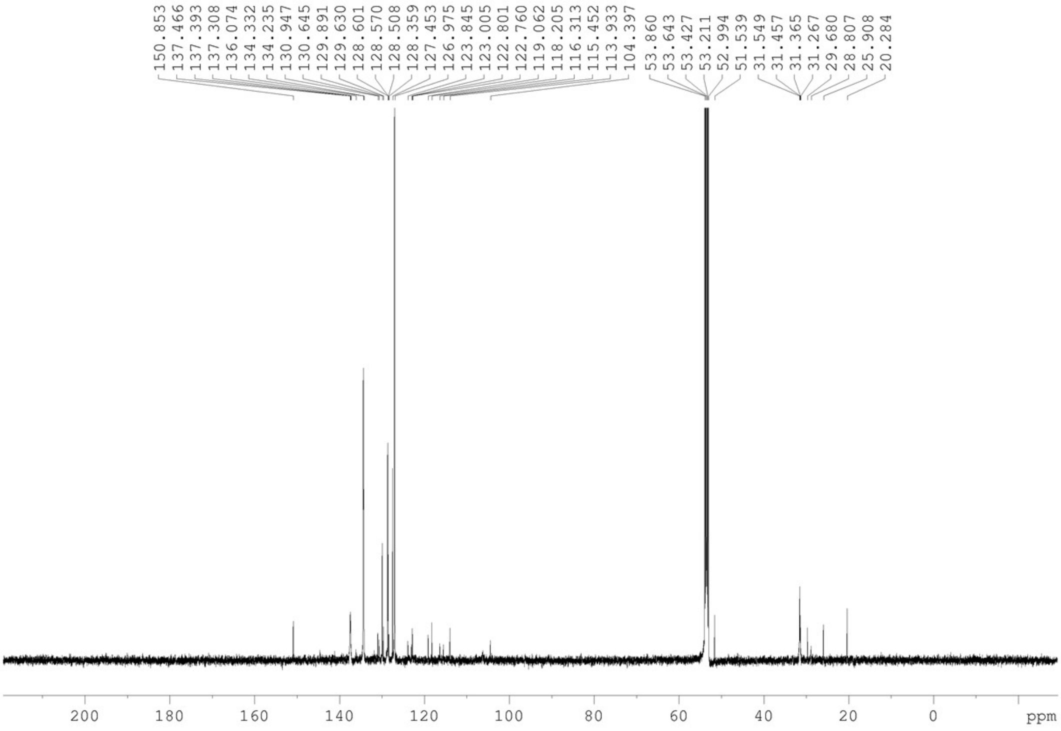

Figure S41 $^{13}C\{^{1}H\}$ NMR (500 MHz) of SP-**13** in CD_2Cl_2

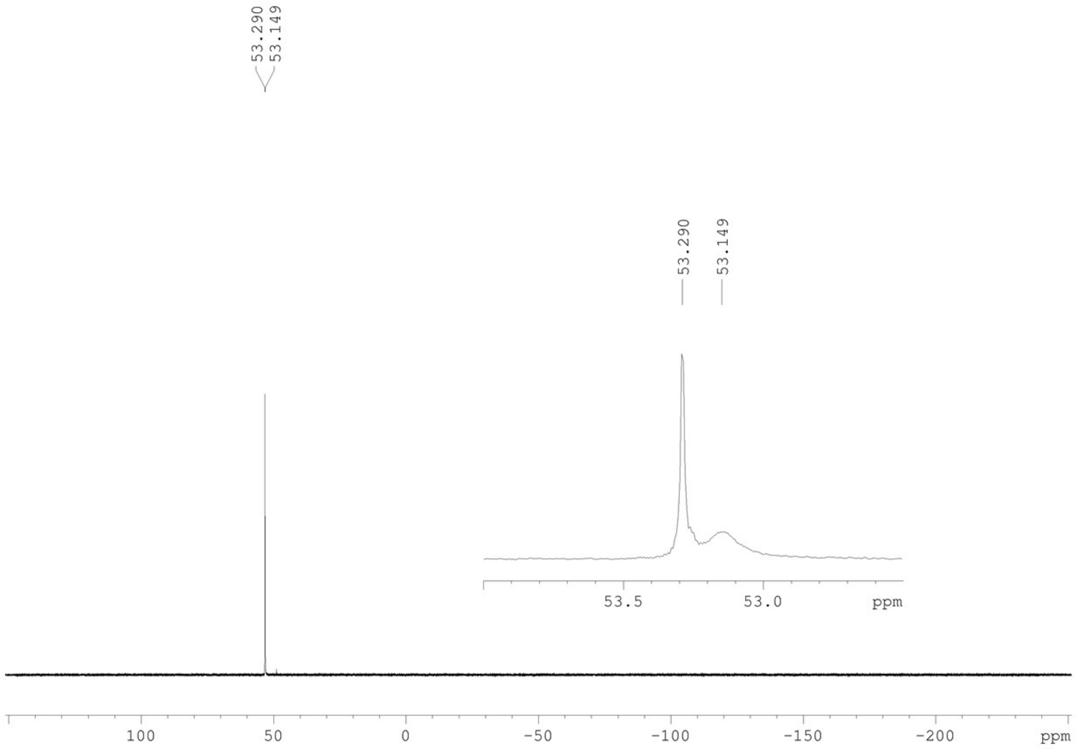

Figure S42 $^{31}P\{^1H\}$ NMR (500 MHz) of SP-**13** in CD_2Cl_2

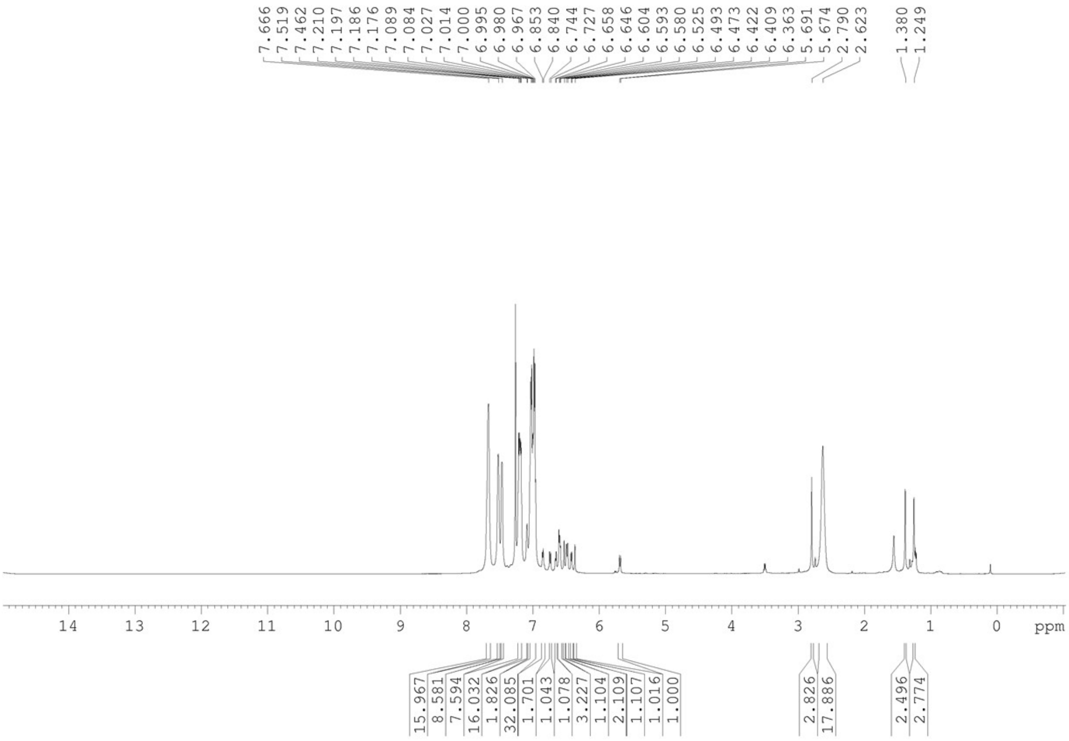

Figure S43 ^1H NMR (600 MHz) of SP-**16** in $CDCl_3$

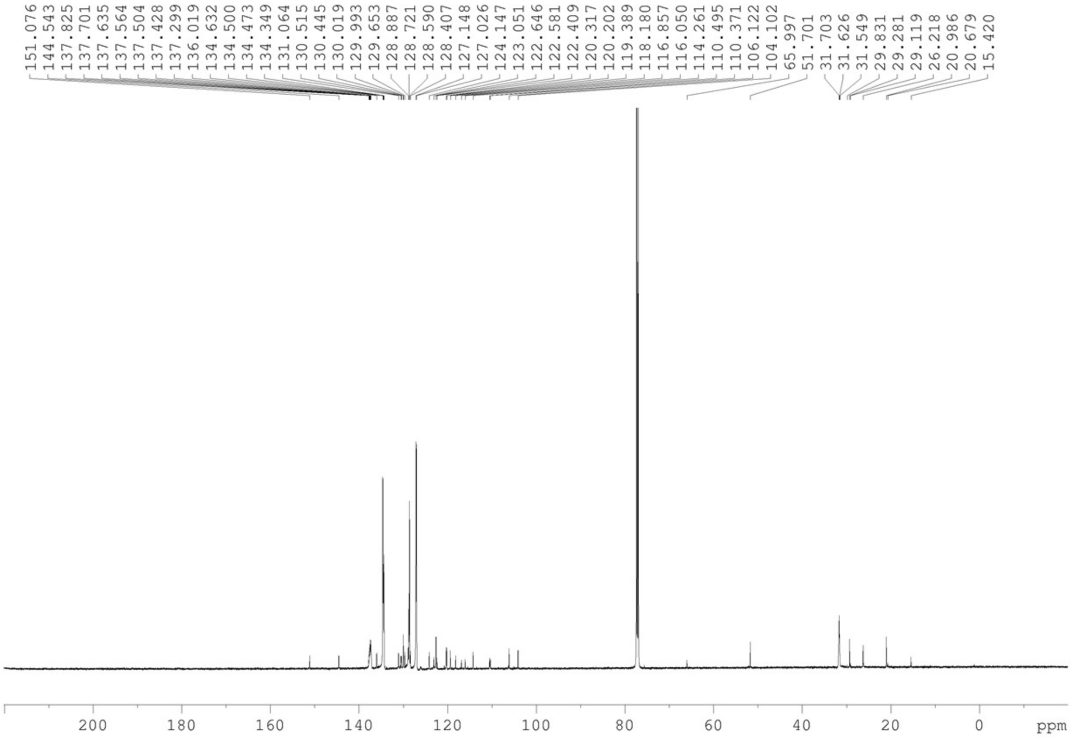

Figure S44 $^{13}C\{^{1}H\}$ NMR (151 MHz) of SP-**16** in CDCl$_3$

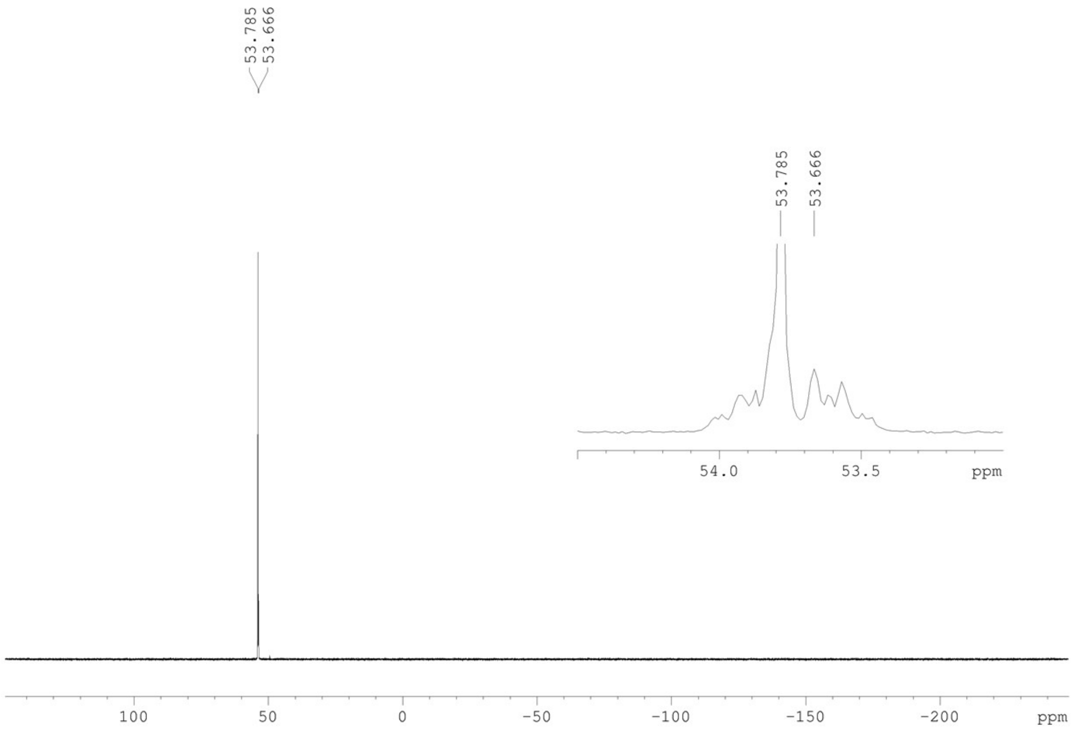

Figure S45 $^{31}P\{^{1}H\}$ NMR (243 MHz) of SP-**16** in CDCl$_3$

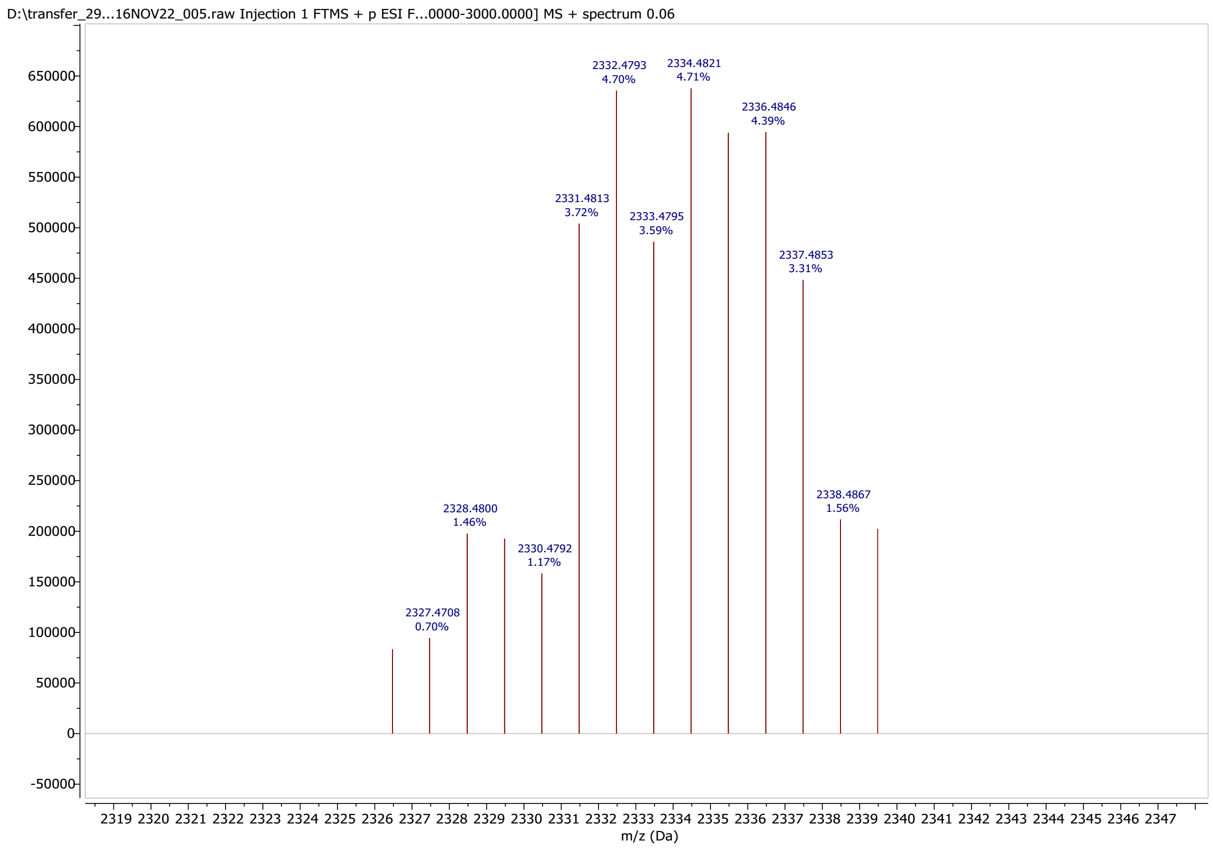

Figure S46 HRMS of SP-**16**.

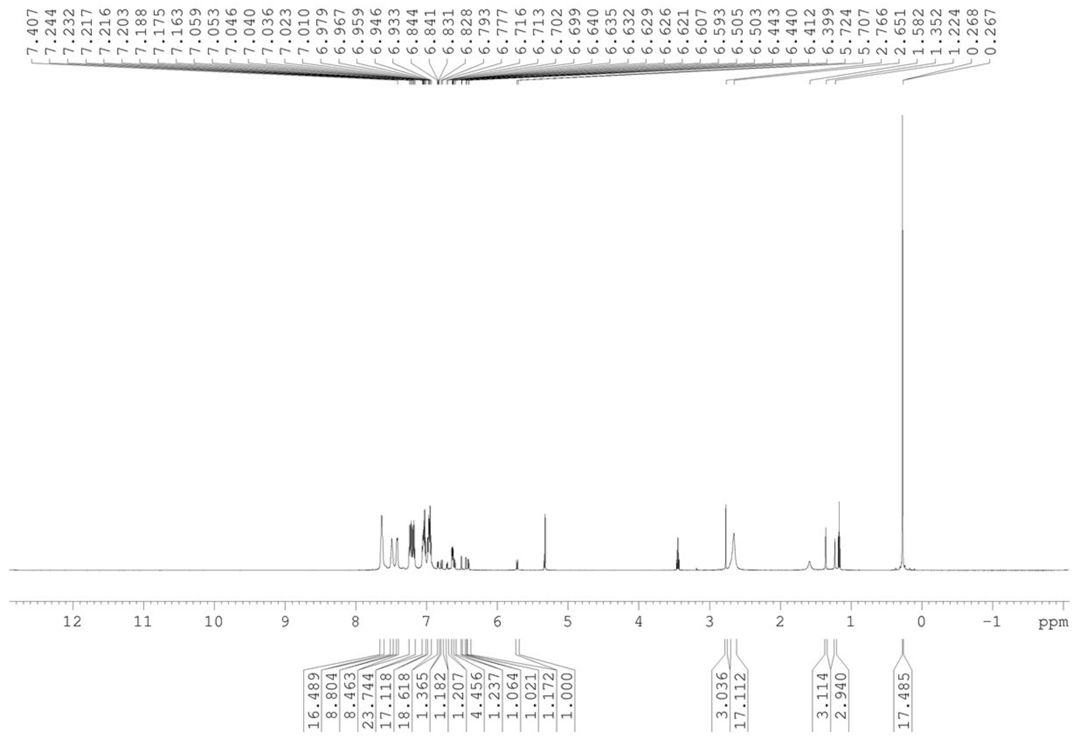

Figure S47 ^{1}H NMR (600 MHz) of SP-**18** in CD_2Cl_2

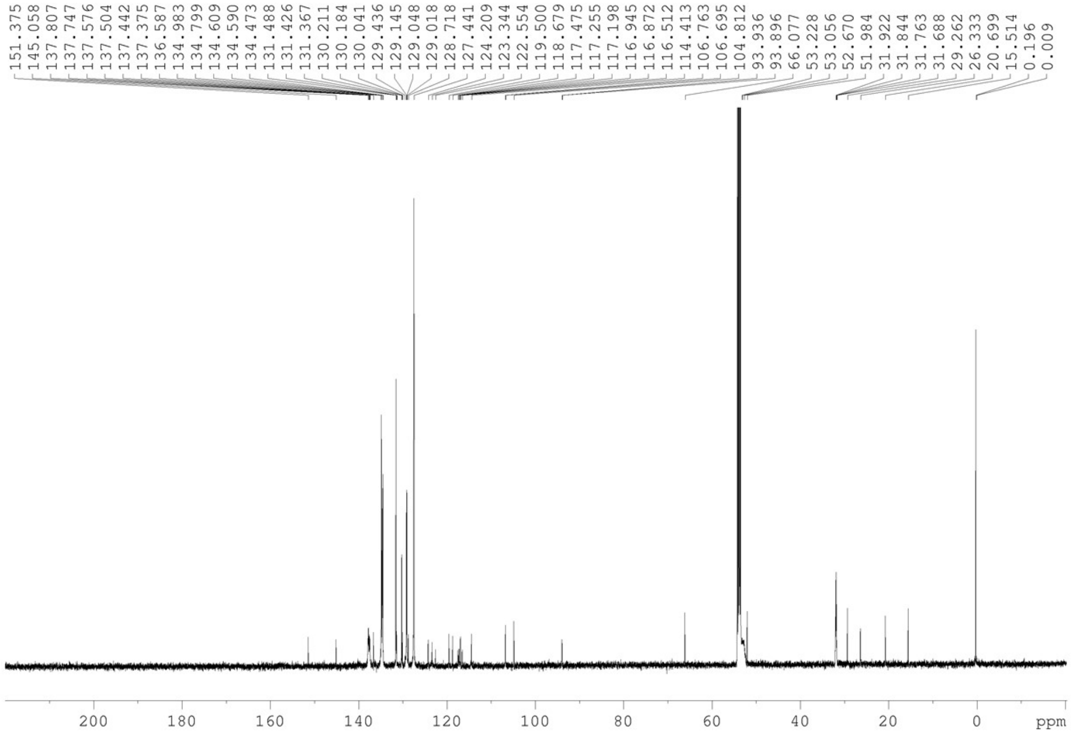

Figure S48 $^{13}C\{^1H\}$ NMR (151 MHz) of SP-**18** in CD_2Cl_2

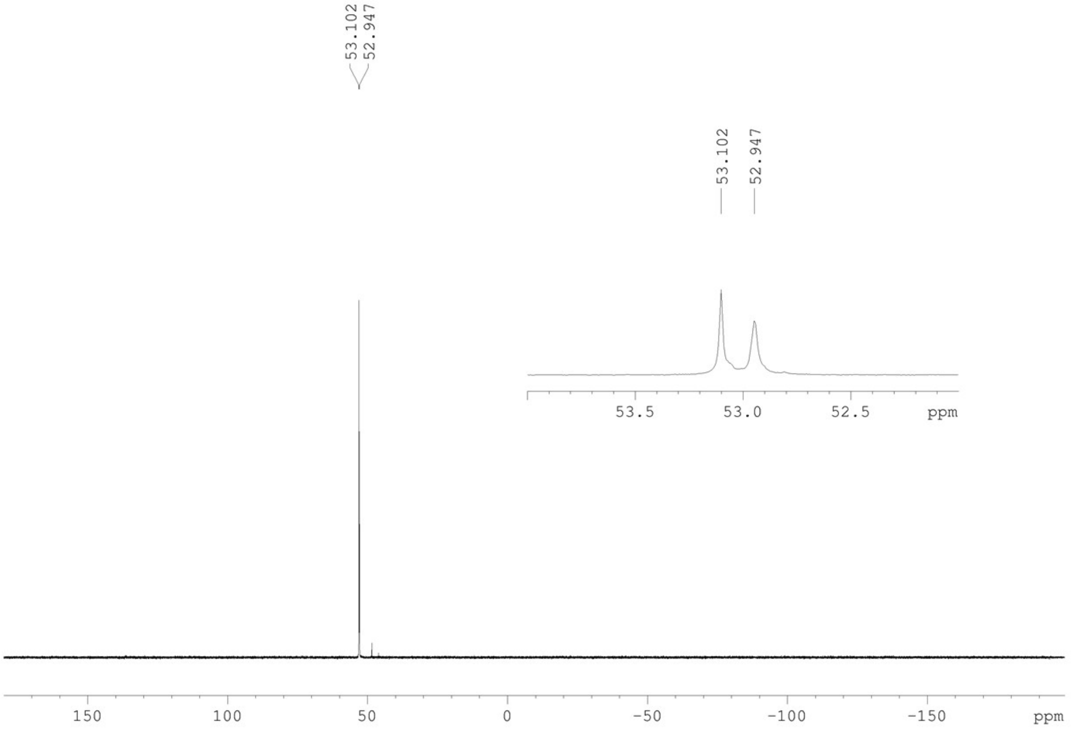

Figure S49 $^{31}P\{^1H\}$ NMR (243 MHz) of SP-**18** in CD_2Cl_2

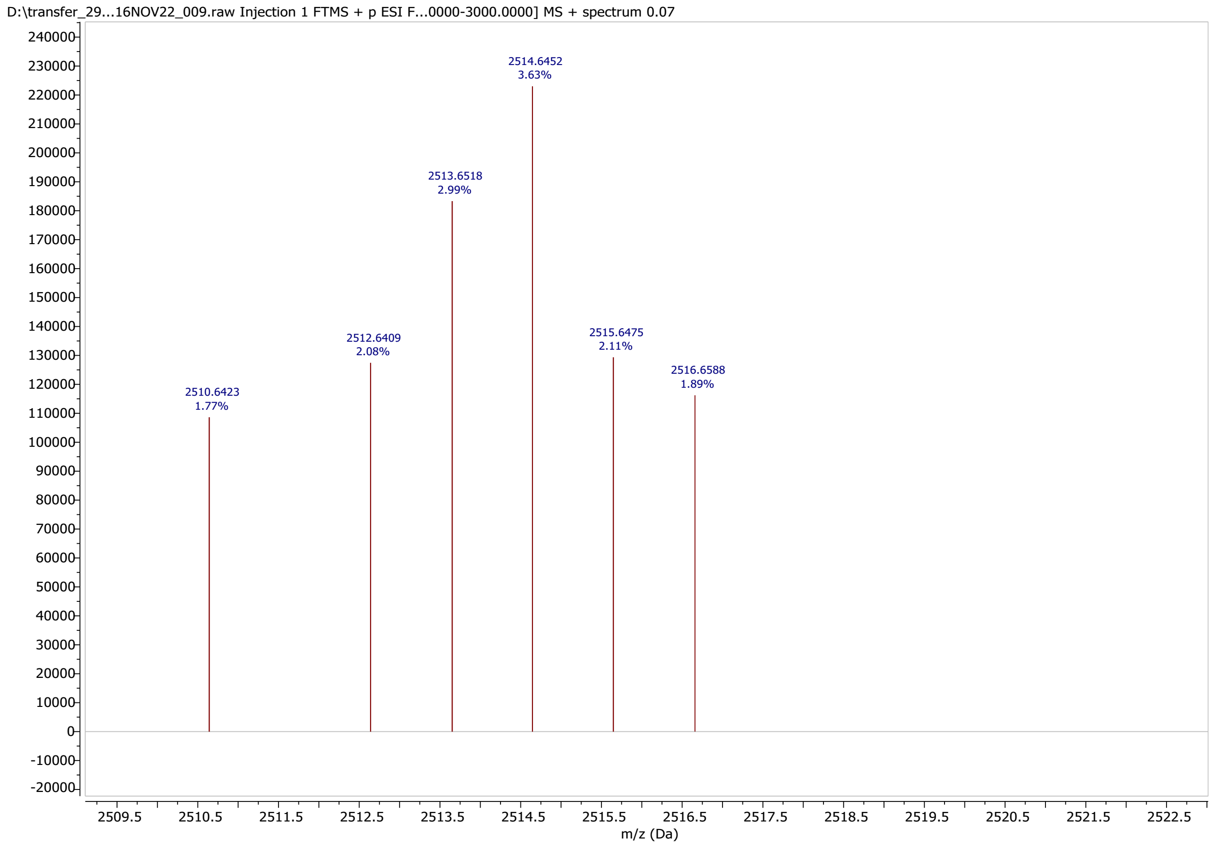

Figure S50 HRMS of SP-**18**.

DFT Calculations

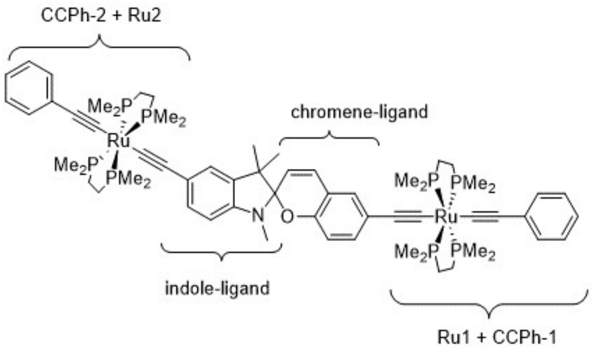

Figure S51 Representation of SP-19 used for DFT calculations.

Table S11. Orbital energy (eV) and composition (%) for selected molecular orbitals of **SP-19**.

MO		eV	CCPh-1	dmpe-1	dmpe-2	Ru1	chromene-ligand	indole-ligand	Ru2	dmpe-3	dmpe-4	CCPh-2
324	L+5	0.89	99	0	0	0	0	0	0	0	0	0
323	L+4	0.86	0	0	0	0	9	88	0	1	0	1
322	L+3	0.75	11	0	0	2	76	9	0	0	0	1
321	L+2	0.49	43	0	0	2	5	3	1	0	1	45
320	L+1	0.48	41	0	0	2	7	4	1	0	1	44
319	LUMO	-0.15	0	0	0	0	95	4	0	0	0	0
318	HOMO	-4.74	1	0	0	2	18	43	21	1	1	12
317	H-1	-4.86	21	1	1	30	40	3	2	0	0	2
316	H-2	-5.17	0	0	0	0	16	7	51	2	2	22
315	H-3	-5.29	26	2	2	43	26	0	0	0	0	0
314	H-4	-5.43	2	0	0	1	3	27	8	3	3	53
313	H-5	-5.58	43	4	4	6	38	2	0	0	0	2

Table S12. Orbital energy (eV) and composition (%) for selected α-spin orbitals of [**SP-19**]$^+$

Alpha MO		eV	CCPh-1	dmpe-1	dmpe-2	Ru1	chromene-ligand	indole-ligand	Ru2	dmpe-3	dmpe-4	CCPh-2
329	L+10	0.97	0	0	0	0	0	2	117	-9	-9	1
328	L+9	0.93	0	0	0	0	0	1	111	-5	-5	0
327	L+8	0.81	99	0	0	0	0	0	0	0	0	0
326	L+7	0.58	26	0	1	3	70	1	0	0	0	0
325	L+6	0.48	0	0	0	0	0	0	0	0	0	99
324	L+5	0.38	70	0	0	3	26	0	0	0	0	0
323	L+4	0.19	0	0	0	0	2	96	0	0	1	1
322	L+3	0.06	0	0	0	0	1	23	3	1	1	72
321	L+2	0.04	0	0	0	0	0	0	38	31	30	1
320	L+1	-0.17	0	0	0	0	4	69	3	0	0	23
319	LUMO	-0.44	0	0	0	0	95	4	0	0	0	0
318	HOMO	-4.98	26	1	1	33	38	1	0	0	0	0
317	H-1	-5.41	26	2	2	45	25	0	0	0	0	0
316	H-2	-5.7	40	4	4	4	37	9	1	0	0	1
315	H-3	-5.8	5	1	1	0	15	62	8	1	1	8
314	H-4	-6.25	0	0	0	0	1	11	4	4	4	77
313	H-5	-6.42	34	14	14	4	35	0	0	0	0	0
312	H-6	-6.5	0	0	0	0	17	7	38	1	1	35
311	H-7	-6.57	0	8	8	83	0	0	0	0	0	0
310	H-8	-6.68	11	5	4	15	60	4	0	0	0	0
309	H-9	-7.05	15	3	3	24	55	1	0	0	0	0
308	H-10	-7.17	0	0	0	0	16	12	4	19	19	29

Table S13. Orbital energy (eV) and composition (%) for selected β-spin orbitals of [**SP-19**]$^+$

Beta MO		eV	CCPh-1	dmpe-1	dmpe-2	Ru1	chromene-ligand	indole-ligand	Ru2	dmpe-3	dmpe-4	CCPh-2
329	L+11	0.97	0	0	0	0	0	2	116	-9	-9	1
328	L+10	0.93	0	0	0	0	0	1	110	-5	-5	0
327	L+9	0.81	99	0	0	0	0	0	0	0	0	0
326	L+8	0.58	25	0	1	2	69	2	0	0	0	0
325	L+7	0.51	0	0	0	0	0	0	0	0	0	99
324	L+6	0.39	59	0	0	3	15	18	1	0	0	4
323	L+5	0.35	10	0	0	1	11	71	1	0	1	5
322	L+4	0.32	2	0	0	0	4	65	4	0	0	24
321	L+3	0.24	0	0	0	0	0	0	40	30	30	0
320	L+2	-0.05	0	0	0	0	3	31	3	0	0	63
319	L+1	-0.43	0	0	0	0	96	4	0	0	0	0
318	LUMO	-3.34	0	0	0	0	17	31	39	1	1	11
317	HOMO	-4.98	26	1	1	33	38	0	0	0	0	0
316	H-1	-5.41	26	2	2	45	25	0	0	0	0	0
315	H-2	-5.7	38	4	4	4	34	8	2	0	0	6
314	H-3	-5.76	7	1	1	0	8	37	8	3	3	33
313	H-4	-6.31	0	0	0	0	17	8	43	1	1	29
312	H-5	-6.42	34	14	14	4	35	0	0	0	0	0
311	H-6	-6.57	0	8	8	83	0	0	0	0	0	0
310	H-7	-6.67	9	4	3	12	55	9	2	1	1	6
309	H-8	-6.7	3	1	1	4	13	28	10	4	4	32
308	H-9	-7.06	15	3	3	23	53	1	0	0	0	1

LUMO+2

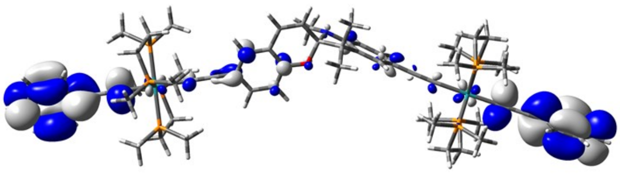

LUMO+1

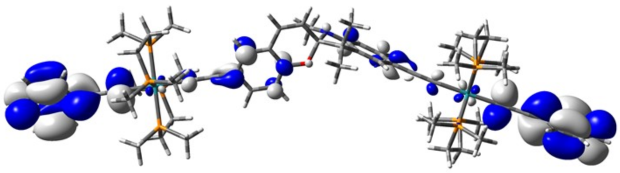

LUMO

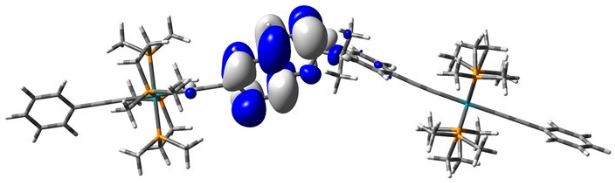

HOMO

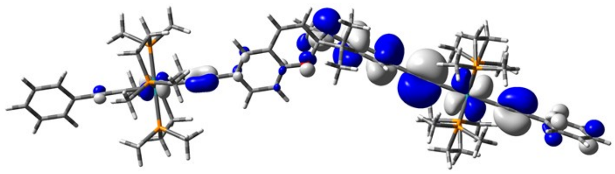

HOMO-1

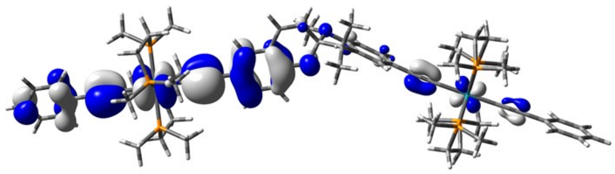

Figure S52 Selected molecular orbitals for **SP-19**.

LUMO(α)+1

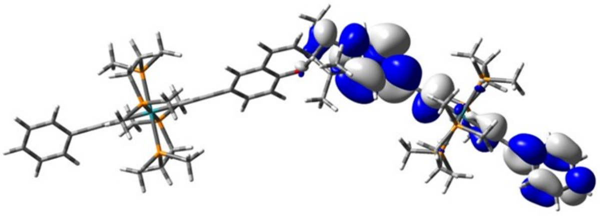

LUMO(β)

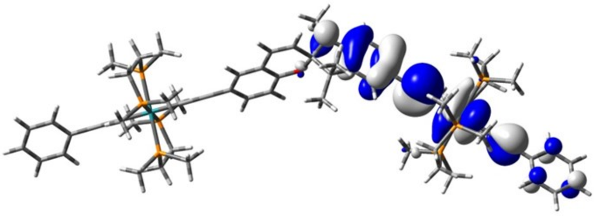

LUMO(α)

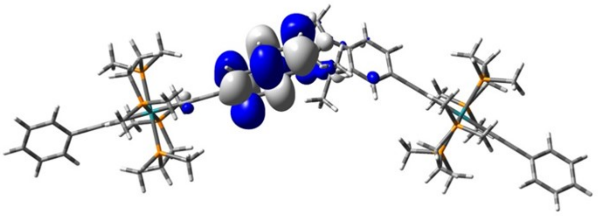

HOMO(β)

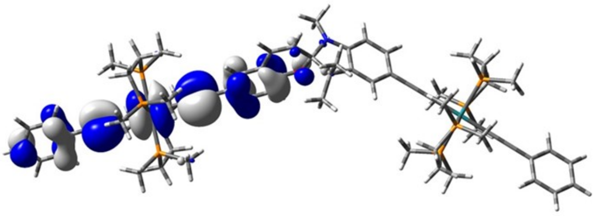

HOMO(α)

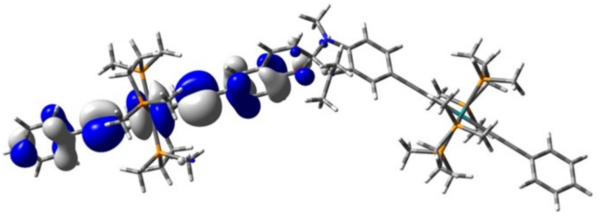

HOMO(β)-3

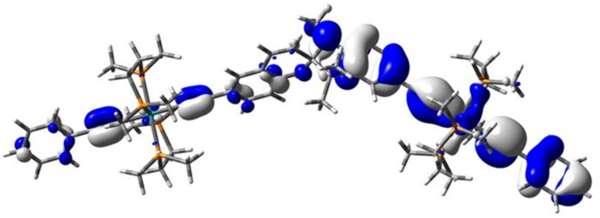

HOMO(α)-3

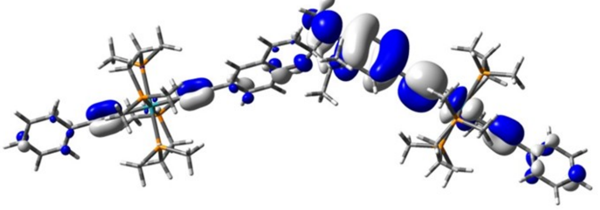

HOMO(β)-9

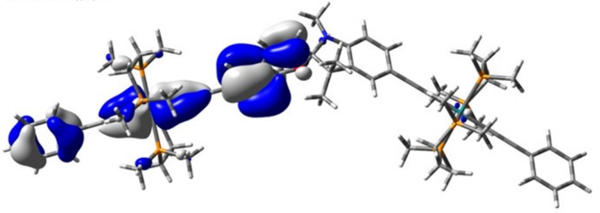

Figure S53 Selected α- and β-spin orbitals for [**SP-19**]$^{+}$.

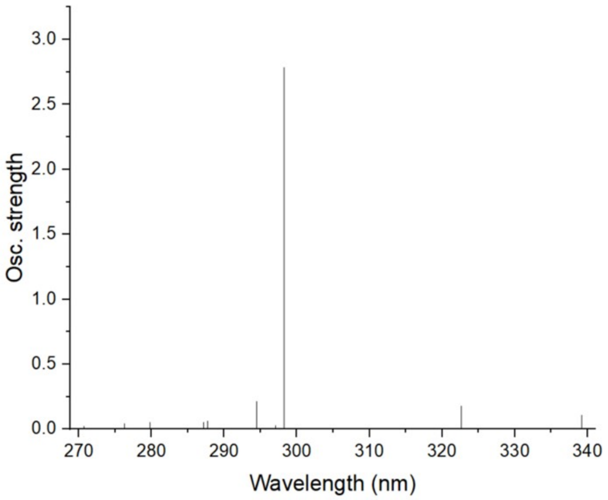

Figure S54 Calculated UV-vis transitions (wavelength versus Oscillator strength) for **SP-19**.

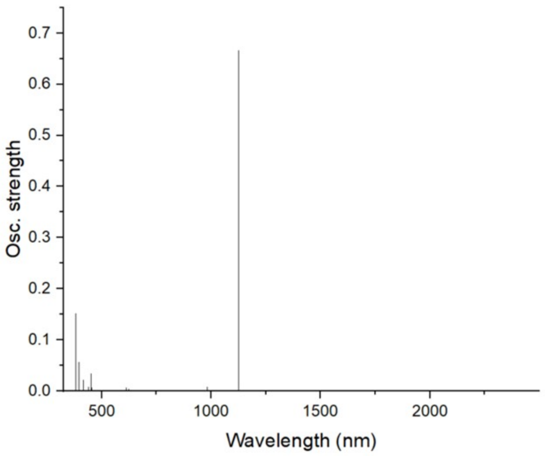

Figure S55 Calculated UV-vis transitions (wavelength versus Oscillator strength) for [**SP-19**]$^+$.

Table S14 Selected major UV-vis transitions for SP-**19** and [SP-**19**]$^+$.

Compound	Energy (cm^{-1})	Wavelength (nm)	Osc. Strength	Symmetry	Major contributor
SP-**19**	33525	298	2.8	Singlet-A	H-1->L+2 (21%), HOMO->L+1 (31%)
[SP-**19**]$^+$	26220	381	0.15	2.484-A	H-3(α)->L+1(α) (16%), H-9(β)->LUMO(β) (49%)
[SP-**19**]$^+$	8874	1127	0.67	2.026-A	H-3(β)->LUMO(β) (72%), H-2(β)->LUMO(β) (17%)